Middle East Journal of Science

www.dergipark.org.tr/mejs

MEJS

VOLUME 6
ISSUE 1

JUNE
2020

E-ISSN
2618-6136

PUBLISHER:
INTERNATIONAL
ENGINEERING, SCIENCE AND EDUCATION GROUP

Email (for orders and customer services enquiries): info@ineseg.org

Visit our home page on www.dergipark.org.tr/mejs

(Prof.Dr., İnönü University, Faculty of Science and Letters, Dep. of Chemistry, Turkey) hkucukbay@gmail.com

20-Hatice Budak GÜMGÜM

Field: Atomic and Molecular Physics, NMR Spectroscopy

(Prof.Dr., Dicle University, Faculty of Science, Dep. of Physics, TURKEY) hbudakg@gmail.com

21-Hüseyin Alkan

Field: Protein Separation Techniques, Pharmacy

(Assoc.Prof.Dr., Dicle UniversityFaculty of Pharmacy, Department of Biochemistry, TURKEY) mhalkan@dicle.edu.tr

22-Ishtiaq AHMAD

Field: Numerical Analysis, Computer Engineering

(PhD., Austrian Institute of Technology, Austria) ishtiaq.ahmad.fl@ait.ac.at

23-İlhan Dağadur

Field: Mathematics, Analysis and Functions Theory

(Prof.Dr., Mersin University Faculty of Arts and Sciences, Dep. of Mathematics, Turkey) ilhandagdur@yahoo.com; idagadur@mersin@edu.tr

24-İsmail Yener

Field: Analytical Techniques, Pharmacy

(PhD., Dicle University, Faculty of Pharmacy, Department of Analytical Chemistry, Turkey) ismail.yener@dicle.edu.tr

25-Javier FOMBONA

Field: Science Education

(Prof.Dr., University of Oviedo, Spain) fombona@uniovi.es

26-Jonnalagadda Venkateswara Rao

Field: Algebra, General Mathematics

(Prof.Dr., School of Science & Technology, United States International University, Nairobi, KENYA) drjvenkateswararao@gmail.com

27-Lotfi BENSAHLA-TALET

Field: Ecology, Hydrobiology

(Assoc. Prof.Dr.,.Department of Biology, Faculty of Natural Sciences and Life, University Oran1-Ahmed BENBELLA, Algeria) btlotfi1977@gmail.com

28-M.Aydın Ketani

Field: Veterinary, Histology and Embryology

(Prof.Dr., Dicle University, Fac. of Veterinary, Dep. of Histology and Embryology, TURKEY)

29-Mukadder İğdi Şen

Field: Astronautics Engineering

(Dr., Trakya University, Edirne Vocational College of Technical Sciences, Turkey) mukaddersen@trakya.edu.tr

30-Murat Aydemir

Field: Inorganic Chemistry

(Prof.Dr., Dicle University, Faculty of Science, Dep. of Chemistry, TURKEY)
aydemir@dicle.edu.tr

31-Murat Hüdaverdi

Field: High Energy and Plasma Physics
(Dr., Yıldız Technical University, Faculty of Science and Letters, Dep. of Physics, TURKEY)
hudaverd@yildiz.edu.tr

32-Müge Sakar

Field: General Mathematics
(Assoc.Prof.Dr., Dicle University, Turkey) mugesakar@hotmail.com

33-Mustafa AVCI

Field: General Mathematics
(Assoc.Prof.Dr., Batman University, Turkey) mustafa.avci@batman.edu.tr

34-Muzaffer DENLİ

Field: Agricultural Sciences, Animal Science
(Prof.Dr., Dicle University, Faculty of Agriculture, Dep. of Animal Sciences, Turkey)
muzaffer.denli@gmail.com

35-Nuri ÜNAL

Field: High Energy and Plasma Physics
(Prof.Dr., Akdeniz University, Faculty of Science, Turkey) nuriunal@akdeniz.edu.tr

36-Özlem GÜNEY

Field: Mathematics, Analysis and Functions Theory
(Prof.Dr., Dicle University, Faculty of Science, Dep. of Mathematics, Turkey)
ozlemg@dicle.edu.tr

37-Petrica CRISTEA

Field: Computational Physics, Condenced Matter Physics, Electromagnetism
(Assoc.Prof.Dr., University of Bucharest, Faculty of Physics, Romania)
pcristea@fizica.unibuc.ro

38-Sanaa M. Al-Delaimy

Field: Atomic and Molecular Physics, General Physics
(Ph.D., Physics Department, Education College for Pure Sciences, Mosul University, Mosul, Iraq) sadelaimy@yahoo.com

39-Selahattin Gönen

Field: Physics Education, Science Education
(Prof.Dr., Dicle University, Faculty of Education, Turkey) sgonen@dicle.edu.tr

40-Şemsettin Osmanoğlu

Field: Atomic and Molecular Physics, ESR Spectroscopy
(Prof.Dr., Dicle University, Faculty of Science, Dep. of Physics) sems@dicle.edu.tr

41-Sezai ASUBAY

Field: Solid State Physics
(Prof.Dr., Dicle University, Faculty of Science, Dep. of Physics, Turkey)
sezai.asubay@gmail.com

42-Süleyman DAŞDAĞ

Field: Biophysics

CONTENTS

Research Articles

INESEG
INTERNATIONAL ENGINEERING SCIENCE AND EDUCATION GROUP

Middle East Journal of Science

https://dergipark.org.tr/mejs

e-ISSN:2618-6136

MEJS

Research Article

X-RAY PROPERTIES OF THE NON-COOL-CORE CLUSTER OF GALAXIES ABELL 2147

Ozden Sengul [1]

[1]Bogazici University Faculty of Education, Mathematics and Science Education Department, İstanbul, Turkey

* Corresponding author: ozden.sengul@boun.edu.tr

Abstract: *XMM-Newton data of the medium-richness non-cD cluster of galaxies Abell 2147, at a redshift of z= 0.035, were analyzed for radial distributions of its X-ray surface brightness, temperature, and metal abundances. The measured X-ray temperature is constant at 5.2 ± 0.8 keV up to ~3' (~ 130 kpc) from the center, while it decreases to ≤ 3.5 keV at ~13' (~ 600 kpc). The obtained abundance profile is consistent with being constant at 0.26 ± 0.08 times the Solar value, although a slight outward decrease is suggested. The X-ray surface brightness can be described by a single β-model, with β= 0.50 ± 0.14 and a core radius of 145" ± 45" = 105 ± 33 kpc. These properties of Abell 2147 agree with those of the best-studies non-cD cluster, Abell 1060. When compared with typical cD clusters, Abell 2147 agrees in its X-ray properties in outer regions, including in particular the outward temperature decrease. However, in the central regions (within ~ 100 kpc), Abell 2147, as well as Abell 1060, lacks major characteristics seen in many cD clusters; the temperature decrease, the abundance enhancements, and evidence for nested two scale lengths in the gravitational potential.*

Keywords: *galaxies, clusters, individual, Abell 2147, X-rays*

Received: May 16, 2020 Accepted: June 9, 2020

1. Introduction

Clusters of galaxies, each containing tens to thousands of galaxies distributed over a typical scale of ~ 1 Mpc, are considered to be the largest gravitationally bound systems in the universe. They are filled with intracluster medium (ICM), namely, the X-ray emitting hot plasma with a temperature of ~ 10^{7-8} K. The ICM, the most dominant known form of cosmic baryons, provides valuable information about the structure and evolution of the clusters of galaxies.

Clusters of galaxies can be classified based on their optical morphology [1]. One of the widely used classification schemes is the Bautz-Morgan classification, which categorizes clusters into objects of Type-I, II, and III. A Type I cluster hosts at its center a predominantly luminous elliptical galaxy, called a cD galaxy. In a Type II cluster, the brightest galaxy is intermediate between typical cD galaxies in Type I systems and normal giant elliptical galaxies. A type III cluster has many elliptical and spiral

galaxies at its core region, and none of them is either centered or dominant. Since Type III clusters lack cD galaxies, they are alternatively called non-cD clusters.

The presence of a cD galaxy in a cluster is known to systematically affect its ICM properties in the central ~ 100 kpc [2]. These include the presence of a bright cool ICM component, a clear central enhancement in the X-ray surface brightness [3], and an increased ICM metallicity. Although these phenomena were once interpreted as evidence of cooling flows [3], the interpretation was thoroughly changed by observations with ASCA [4], and with subsequent X-ray missions [5-7]. The central ICM temperature decrease in these objects is now understood as a result of the stable co-existence of hot and cool plasma [8], and the central excess brightness is considered to reflect hierarchical potential shapes around cD clusters [7,9].

Non-cD clusters, in contrast, generally lack these phenomena that are common to cD clusters. In particular, the ICM in a non-cD system is more isothermal even at the center, with weaker or no evidence of the cool component [4]. At present, the origin of the marked differences between the two types of clusters is not well understood. They may represent different stages of cluster evolution. Or else, they could be different from the beginning of their lifetime, due to fluctuations in the initial conditions of cosmological structure formation. To address this issue, we need to more thoroughly understand X-ray differences between the two cluster types. Since cD clusters have been relatively well studied, we should focus on clarifying the X-ray properties of non-cD clusters.

Abell 1060 (at a redshift of z= 0.011), with a relatively circular shape [10], is by far the best studies non-cD cluster. In addition to early ASCA results [6], recent observations of this object, with Chandra [11], XMM-Newton [12], and Suzaku [13], revealed that its ICM is nearly isothermal at ~ 3.4 keV over the central region within ~75 kpc, with a mild outward temperature decrease. Given this, it is important to examine other non-cD clusters in comparison with Abell 1060 on one hand, and with cD clusters on the other hand. Additionally, there is a recent catalogue study for clusters of galaxies which includes A2147 as well [14]. ROSAT observations showed that the global properties for temperature, morphology of the extend gas beta profile are studied and temperature and beta values are given respectively, kT = 5.2 $\pm$ 0.8 keV temperature, β= 0.50 ± 0.14 Solar, and core radius of r_c=105 ± 33 kpc consistent with the literature values for A2147 (kT = 3.81 ± 0.10 keV, β = 0.36±0.02 Solar and r_c = 85.48 ± 20.0 respectively) [14].

In the present paper, we analyzed an archival Abell 2147 (hereafter A2147), which is a nearby (z= 0.035), relaxed, non-cD cluster with a Bautz-Morgan Type III. It is devoid of a cD galaxy, and none of its three bright central galaxies coincides in position with the X-ray centroid. There is no evidence for any merging at its center. Its temperature profile was surveyed with ASCA, ROSAT, and Chandra. However, these works both dealt with a large sample of clusters, and hence information Newton data set of A2147. Utilizing the large effective area and good angular resolution of XMM-Newton, we successfully measured the temperature and abundance profiles out to a radius of ~ 600 kpc. Throughout this paper, we assume the Hubble constant to be H_o= $70h_{70}$ km s^{-1} Mpc^{-1}, and employ the cosmological parameter Ω_M= 0.27. Thus, at z= 0.035, 1' corresponds to 43.5 kpc. The Galactic line-of-sight absorption towards A2147 is taken as N_H= 3.2 x 10^{20} cm^{-2}. Unless stated otherwise, errors represent 90% confidence limits.

2. Material and Methods

2.1. XMM-Newton observation and data reduction

The present XMM-Newton observation of A2147 was carried out on 2007 August 3 for a new exposure of 12 ks. All the EPIC cameras were operated in the full-frame mode with a medium filter inserted. The data reduction and analysis were performed with the SAS version 10.0.0. For better use of Extended Source Analysis Software (ESAS), the patched versions, SAS 10.0.1 and SAS 10.0.2 were reinstalled after their release.

Unfortunately, the present data were significantly affected by soft protons. Therefore, we filtered the calibrated event files using several tasks ("mos-filter", "pn-filter" and "espfilt") in the ESAS package. These tasks identify those time periods when the proton contamination is considered to be significant, and discard all events therein. This time filtering was done in units of 100 s as a default setting. This process left us with ~ 8 ks of good time intervals out of the original 12 ks.

2.2. Subtraction of Backgrounds

Figure 1 (a) shows, in black, the 0.5-12 keV on-source spectrum, derived from the time-filtered EPIC MOS2 data within a region of radius r= 13'. For background subtraction, we first used blank-sky data sets, which we obtained from the XMM-Newton EPIC "Blank Sky" Background website where a large amount of blank-sky data of various observing conditions are available. An event file with a total exposure of 363 ks was created, under conditions of the medium filter and full-frame mode.

The red spectrum in figure 1 (a) shows the background spectrum, this accumulated over the same spatial region. The difference between the two spectra primarily represents celestial signals, including the cluster emission and the cosmic X-ray background. The two prominent features at ~ 1.49 keV and ~ 1.75 keV are both instrumental, fluorescent Al-Kα, and Si-Kα lines, respectively. The on-source spectrum becomes close to the background toward high energies. However, as shown in figure 1 (b), the former remains higher by ~30% than the latter even above ~10 keV, where the cluster emission should be negligible. This indicates that the soft proton contamination has not been completely removed by the time filtering. Presumably, prominent "flares" in the light curve were removed, while relatively constant soft protons were not.

To remove the residual soft-proton background, we resorted to another method. Namely, we created model background spectra using the "mos-back" task in the XMM-EASA package. The modeling was done for each detector and CCD individually. This ESAS-created background is shown in Figure 1 in green. Since it is mainly meant to reproduce the effects of relatively constant high-energy particles [15], it includes neither cosmic X-ray background (CXB) nor the instrumental fluorescent lines; these must be modeled separately. Although the model background thus predicts somewhat higher counts in the 10-12 keV range than the previous blank-sky data, the on-source data therein are still higher than this by a factor of ~ 1.16. Considering these, we have finally chosen to increase, by the same factor, the ESAS model.

The same analysis, performed on the MOS1 and PN data, gave Figure 2. Thus, the on source 10-12 keV MOS1 data exceed the ESAS background by a factor of ~1.5, and hence we had to increase the background by 50%. In contrast, such a background re-adjustment was not necessary for the PN data, because the ESAS background agrees well with the data over the 10-12 keV range.

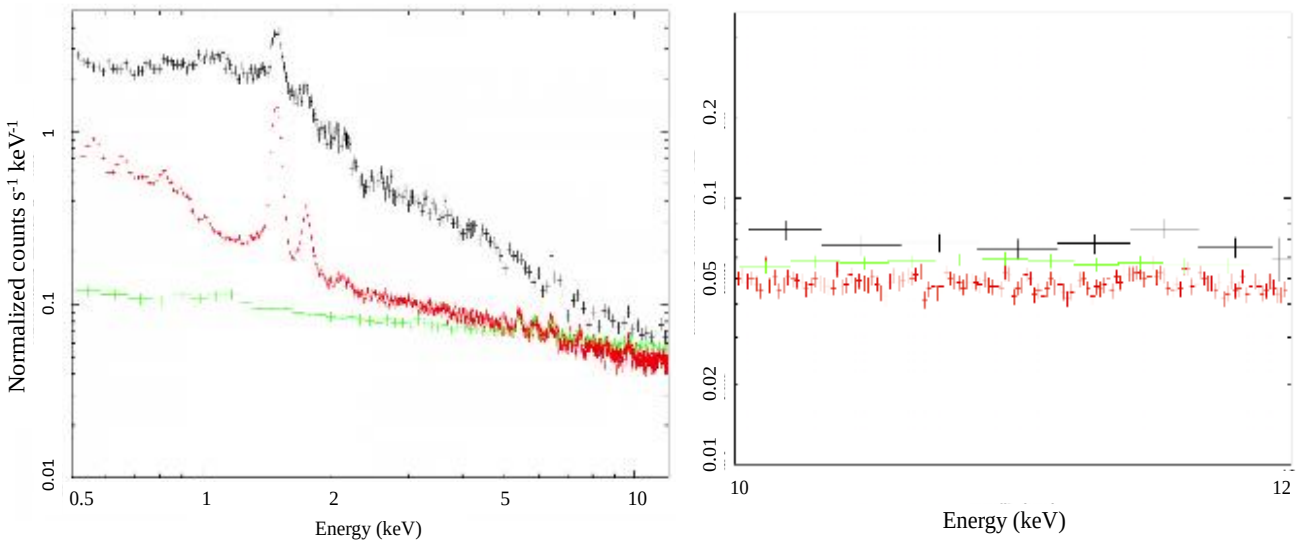

Figure 1. (Left) A raw spectrum of A2147 (black) at 0.5-12 keV, accumulated over a radius of r≤ 13' using the time-filtered MOS2 data, compared with the blank-sky background (red) and the ESAS created model background (green). Right spectrum at 10-12 keV.

The CXB contribution to our data was estimated by the "fake" command using uniform-sky response matrices, assuming that the whole sky has a uniform brightness. According to Kushino et al. (2002) [16], the CXB is characterized by a photon index of $\Gamma = 1.412 \pm 0.007 \pm 0.025$ and an average 2-10 keV brightness of $(6.28 \pm 0.04 \pm 0.64) \times 10^{-8}$ erg cm^{-2} s^{-1} str^{-1}. We hence subtracted the CXB in our data using a model that has a proton index of $\Gamma = 1.4$ and a 2-10 keV surface brightness of 6.57×10^{-9} erg cm^{-2} s^{-1} sr^{-1}, absorbed by the Galactic line-of-sight column of $N_H = 3.2 \times 10^{20}$ cm^{-2}.

The background-subtracted data are subject to both statistical (Poisson) and systematic errors. The latter is dominated by uncertainties in the level of the background to be subtracted. In Figure 1, each data point in the on-source data has a typical 1σ statistical error of ± 10%. Since we have 8 data points, the background adjustment can be done with a 1σ accuracy of ±3%. We hence quote this as the systematic error associated with the signal spectra.

2.3. Preparation of spectra

Figure 3 shows a background-inclusive 0.5-10 keV image of A2147 derived with MOS2. From the image, the X-ray center of A2147 was determined as the brightest point at (α, δ)= ($16^h02^m14.4^s$, 15^o 58' 07".50). Around this centroid, we divided the MOS1 and MOS2 images into eight concentric annular regions, with radii of 0'-1'.0, 1'.0-2'.0, 2'.0-3'.0, 3'.0-4'.5, 4'.5-5'.6, 5'.6-7'.0, 7'.0-10'.0 and 10'.0-13'.0. The innermost radii were determined considering the angular resolution of XMM-Newton (~10"), while outer regions were set progressively wider in order to approximately retain statistics.

We accumulated MOS1, MOS2, and PN spectra over the individual annuli (eight for MOS and six for PN). Then, the re-adjusted ESAS model background and the modeled CXB were subtracted. Each background-subtracted spectrum was fitted with a single APEC model, in which the temperature, abundance, and the spectrum normalization were left free. The source redshift was fixed at 0.035, and the hydrogen column density at 3.2×10^{20} cm^{-2}. To reproduce the instrumental Al-Kα and Si-Kα lines, which are present in the data but not in the employed background model, two narrow Gaussians were

added at 1.49 keV and 1.75 keV, respectively, with their normalizations left as free parameters. In this way, the MOS and PN spectra were fitted separately in 0.5-10.0 keV and 0.5-7.0 keV, respectively.

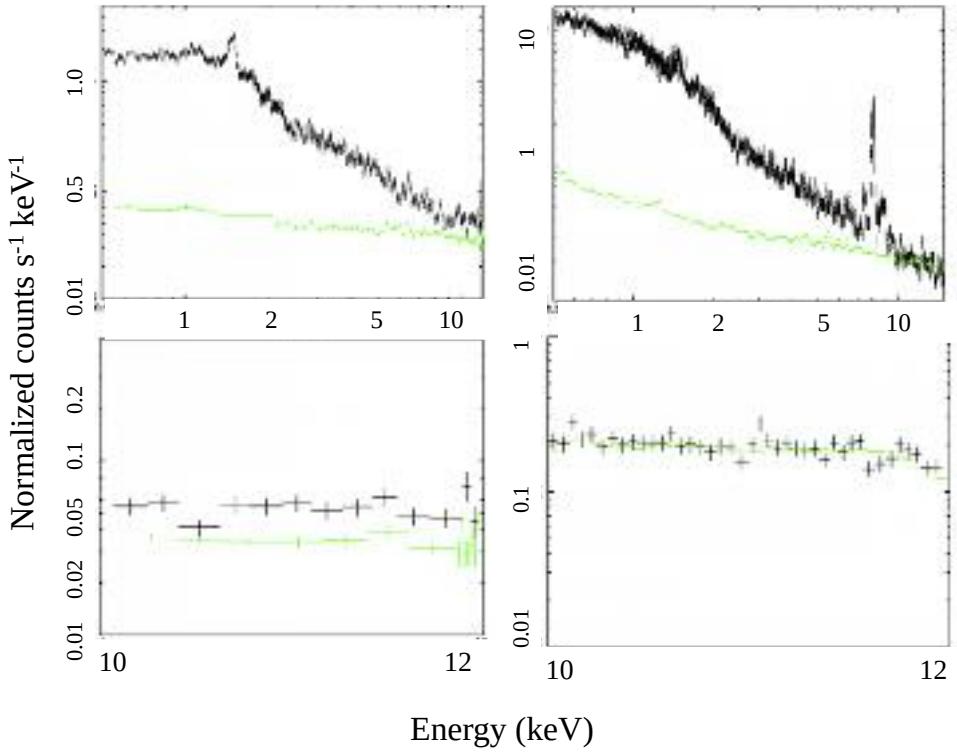

Figure 2. MOS1 (left) and PN (right) spectra (black) of A2147, both accumulated over r≤ 13', compared with the ESAS-created background (green). The bottom panel is an expanded view of the 10-12 keV region of the top panel.

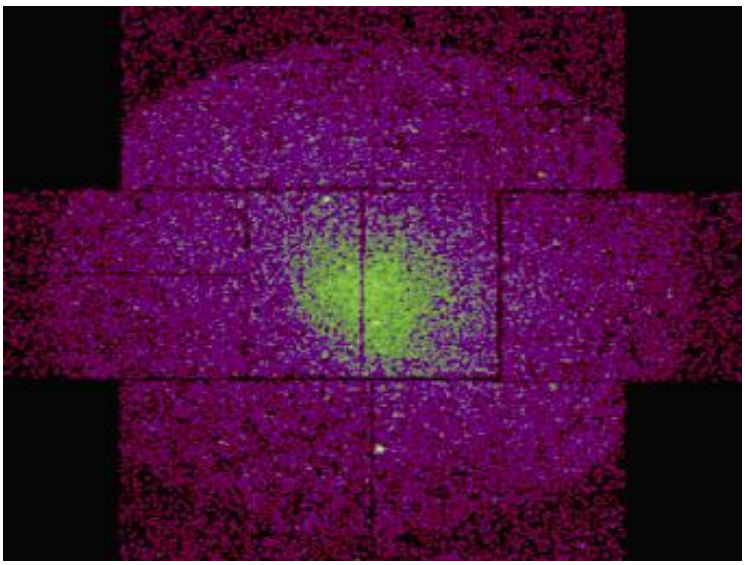

Figure 3. A background-inclusive 0.5-12 keV raw image of A2147 with MOS2.

2.4. Soft Excess Component

Several results of this single-APEC fit are shown in Figure 4. Thus, the fits were generally unacceptable; for example, the MOS2 spectra from the inner to outer annuli gave χ^2/ν= 0.91, 1.29, 1.33, 1.46, 1.36, 1.45, 1.42 and 1.76, typically with $\nu \sim 60$ degrees of freedom. As can be seen in Figure 4, the data are more concave than the model, showing "soft excess" at ≤ 1 keV.

The XMM-Newton data are often contaminated by the so-called Galactic foreground emission (or magnetospheric foreground due to Solar-wind charge-exchange) [16] which appears as a soft thermal emission in energies ≤ 2 keV with a nearly constant brightness across the EPIC FOV. Its typical intensity at 0.5 keV, ~ 1.0 cts s^{-1} keV^{-1} when integrated over the EPIC FOV much exceeds the ESAS background (~ 0.12 cts s^{-1} keV^{-1}) plus the CXB (~ 0.10 cts s^{-1} keV^{-1}). Then, the soft excess seen in Figure 4 may be caused by this phenomenon. However, we need a caution, because cool cluster emission, if any, would produce similar effects.

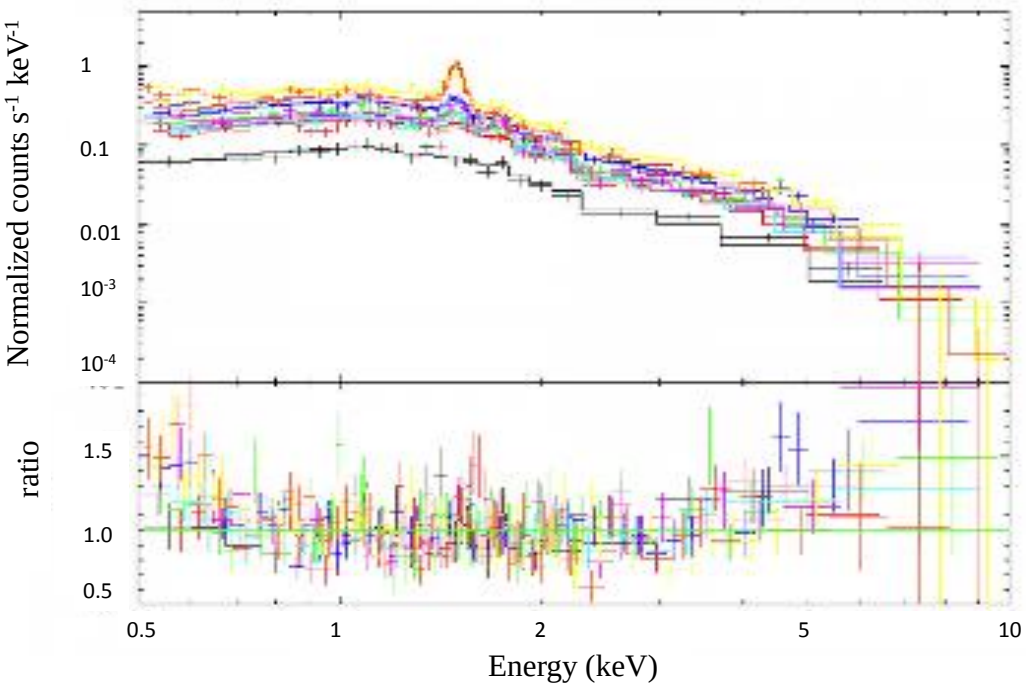

Figure 4. The individual fits the background-subtracted MOS2 spectra from the eight annular regions.

The employed model is an absorbed single APEC component. Data from the inner to outer regions are shown in black, red, cyan, green, magenta, blue, orange, and yellow. The bottom panel summarizes the data to model ratios. To examine whether the soft excess component in the present A2147 data is intrinsic to the cluster or due to a foreground (either Galactic or magnetospheric) emission, we show, in the bottom panel of Figure 4, the ratio of each annular spectrum to its best-fit model. Thus, the soft-excess strength, relative to a single thermal model approximating the cluster emission, is clearly stronger in outer regions (yellow, orange, and blue) than in inner regions (black, red, and magenta), implying that the soft excess has a much flatter brightness distribution than the ICM emission. Therefore, the soft excess must be dominated by foreground contamination, rather than by a cool component in the cluster emission.

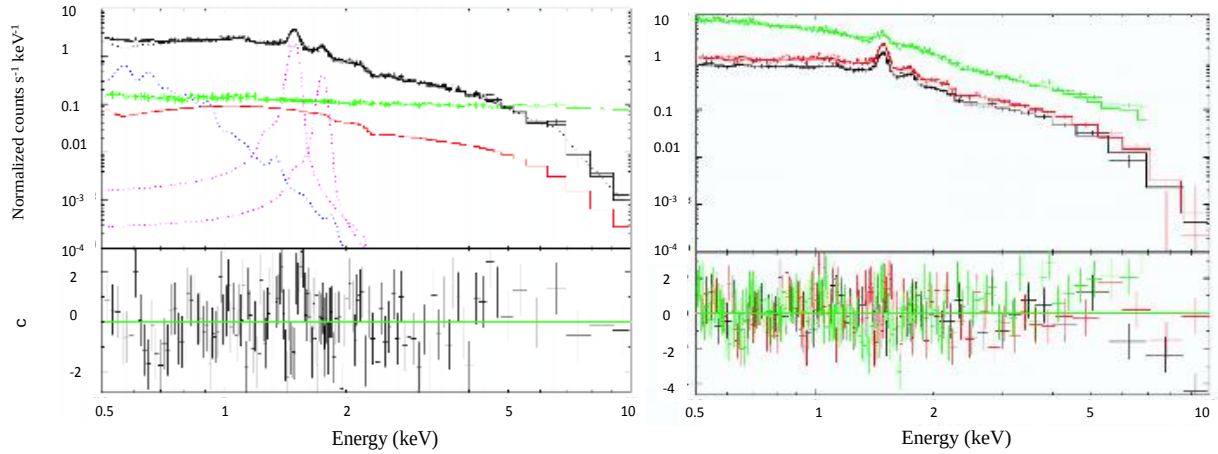

Figure 5. (a) (left) The cluster-averaged MOS2 spectrum within r = 13', decomposed into the ICM emission (black; a single APEC model), Al-Kα and Si-Kα lines (magenta), and the foreground emission (blue). The fit yielded $\chi^2/\nu = 1.12$. The ESAS background (green) and the CXB (red), which were both already subtracted before the fitting, are restored for comparison. (b) (right) MOS1 (black), MOS2 (red), and PN (green) spectra from their respective optimum regions for the soft-excess determination (excluding the core regions; see text) fitted simultaneously by a double APEC model. The two instrumental features at ~ 1.5 keV and ~ 1.75 keV are modeled by narrow Gaussians. The bottom panel shows the fit residuals.

To further quantify the soft excess component, we accumulated MOS1, MOS2, and PN spectra over radius ranges of 4'.5-13'.0, 5'.6-13'.0 and 4'.5-13'.0, respectively. To approximately maximize the statistics for the soft excess spectrum, we excluded the central region, where the ICM emission is too bright and a cool ICM emission could possibly be present. Then, the three spectra were fitted simultaneously by a double APEC model, the hotter one describing the cluster emission and the cooler one the soft excess. The two APEC temperatures, as well as the hotter APEC abundance, were allowed to float but constrained to be the same among the three spectra. The cooler APEC component was assumed to have a 1 solar abundance. The two APEC normalizations were allowed to take free values, which depend on the camera. The fit χ^2 was calculated by summing over the three spectra. As shown in Figure 5(a), the fit was acceptable ($\chi^2/\nu = 1.12$ with $\nu = 698$), and has yielded a cooler APEC temperature of 0.21 ± 0.02 keV, which is reasonable for a Galactic (or magnetospheric) foreground emission.

2.5. Cluster-averaged spectra

Now that the foreground soft excess in the present sky direction has been quantified, let us determine the cluster-averaged ICM temperature, including the bright core regions which were excluded in Figure 5(a). For this purpose, we prepared another background-subtracted MOS2 spectrum over the field of view, $r \leq 13'$, and fitted it, using a model of wabsx (apec+apec+gauss+gauss). Here again, the second APEC component represents the foreground soft excess, with a temperature fixed at 0.21 keV. Its normalization was also fixed to a value which is scaled from the fitting results of figure 5(a). Here and hereafter, the spectral fits all incorporate systematic errors by 3% of the particle background.

As shown in figure 5(b), this model has given an acceptable fit to the cluster-averaged MOS2 spectrum with $\chi^2/\nu = 1.12$ for $\nu = 698$. Similarly, the FOV-integrated MOS1 and PN spectra were fitted

successfully. The ICM temperatures and the abundances, thus determined separately by the 3 cameras, are given in the last column of table 1 and table 2, respectively. Since the three cameras thus give mutually consistent results, we also performed a simultaneous fitting to the three spectra, and again obtained a successful fit (see table 1 and table 2). The combined temperature derived from a simultaneous fitting to the three (MOS1, MOS2, and PN) spectra, 4.44 $\pm$ 0.30 keV, is consistent with the previous reports.

3. Results

3.1. Radial temperature and abundance profiles

The individual annular spectra from each camera were fitted by the same model as above, in which the soft-excess parameters are again fixed to the values determined with Figure 5(a). The innermost PN spectrum averages over 0'-3', while this range is divided into three for the MOS data. As exemplified in Figure 6, the fits were generally acceptable and yielded the fit parameters as summarized in Table 1 (the temperature and the fit chi-square) and Table 2 (the metal abundances). Finally, the spectra from the three (or two) cameras were fitted simultaneously. The results are also given in the two tables.

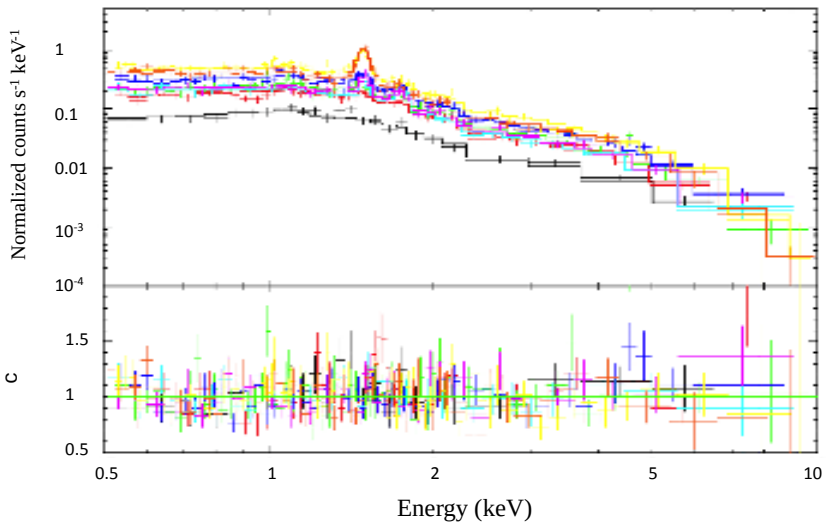

Figure 6. The individual fits the eight annular spectra of the MOS2 camera. The model describes the ICM emission with a single APEC component and the soft excess with another APEC.

Figure 7(a) shows the radial temperature profiles, determined jointly by the three (or two) cameras. Thanks to the large effective area of XMM-Newton, we have thus been able to measure the ICM temperature of A2147 up to r=13', or ~ 600 kpc. The results indicate a gradual outward temperature decline. Specifically, it is constant at 5.20 $\pm$ 0.75 keV up to r ~ 3', or 130 kpc, while it decreases to $\leq$ 3.5 keV at r ~ 13', or 600 kpc. This temperature gradient is significant because we obtain $\chi^2/\nu = 5.3$ ($\nu = 7$) if the data points in Figure 7(a) are fitted with a constant. Similarly, Figure 7 (b) shows the obtained abundance profiles, where a mild outward decrease is suggested. However, a fit to these 8 data points with a constant yield $\chi^2/\nu = 0.7$ ($\nu = 7$). Therefore, the data are consistent, within errors, with a spatially constant abundance. To be more quantitative, a power-law fit to the data points, with a function of $\alpha\ r^{\alpha}$, gave a slope as $\alpha = -0.6 \pm 0.41$, where the errors refer to 1-sigma (68%) confidence limits. Thus, $\alpha = 0$ (no gradient) is still allowed, even though the data prefer a negative slope.

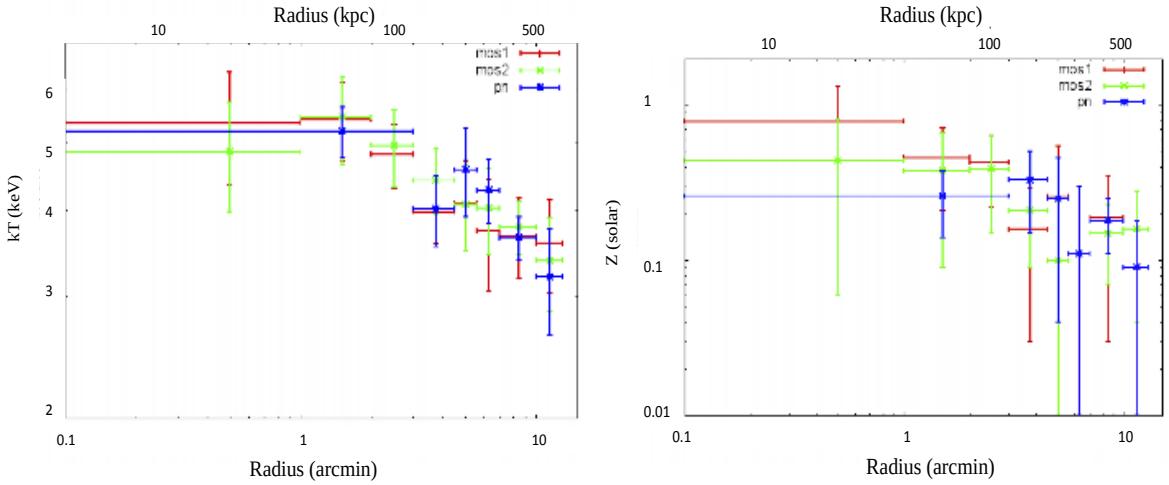

Figure 7. Temperature (panel a) and abundance (panel b) profiles of A2147, determined by joint fittings to the data of the three cameras. Errors refer to statistical (68%- 1 sigma) plus systematic ones

Table 1. The ICM temperatures measured at individual annular regions*

Radius	MOS1	χ^2/ν	MOS2	χ^2/ν	PN	χ^2/ν	Combined
0'-1'	5.34±0.99	0.80	4.86±0.88	0.89			5.08±0.93
1'-2'	5.41±0.70	1.28	5.45±0.79	1.17			5.43±0.74
2'-3'	4.81±0.51	0.78	4.95±0.64	1.12	5.20±0.44	1.10	4.86±0.58
3'-4'.5	3.98±0.41	1.11	4.42±0.48	1.07	4.01±0.47	0.94	4.11±0.45
4'.5-5'.6	4.10±0.61	0.85	4.07±0.58	0.92	4.58±0.67	0.94	4.28±0.62
5'.6-7'	3.74±0.69	0.92	4.02±0.57	1.00	4.27±0.45	1.19	4.08±0.57
7'-10'	3.67±0.49	1.37	3.78±0.33	1.02	3.65±0.26	1.20	3.69±0.36
10'-13'	3.58±0.55	1.11	3.38±0.52	1.14	3.20±0.56	1.24	3.29±0.54
0'-13'	4.62±0.28	1.08	4.21±0.28	0.99	4.48±0.35	0.98	4.44±0.30

*Errors refer to statistical plus systematic uncertainties

Table 2. The ICM abundances (Solar units) measured at individual annular regions*

Radius	MOS1	MOS2	PN	Combined
0' – 1'	0.79±0.53	0.44±0.38		0.56±0.45
1' – 2'	0.46±0.25	0.38±0.29		0.42±0.27
2' – 3'	0.43±0.21	0.39±0.24	0.26±0.12	0.41±0.22
3' – 4'.5	0.16±0.13	0.21±0.12	0.33±0.18	0.22±0.14
4'.5 – 5'.6	0.26±0.26	0.10±0.10	0.25±0.21	0.14±0.19
5'.6 – 7'	0.11±0.11	0.08±0.08	0.11±0.11	0.10±0.10
7' – 10'	0.19±0.16	0.15±0.08	0.18±0.07	0.17±0.10
10' – 13'	0.06±0.06	0.16±0.12	0.09±0.09	0.08±0.09
0' – 13'	0.24±0.12	0.21±0.06	0.34±0.07	0.26±0.08

*Errors refer to statistical plus systematic uncertainties

3.2. X-ray Surface Brightness Profiles

A surface brightness profile, extracted from an X-ray image, usually decreases monotonically from the center to the periphery and carries information on the underlying potential shape. Using the "Funtools[2] (FITS Users Need Tools)" software, we extracted the X-ray surface brightness from the background-subtracted 0.4-8 keV MOS2 image and corrected it for exposure (including the effect of

vignetting). Like in the spectrum analysis, the ESAS background was subtracted after correcting for the vignetting and multiplying by the factor of 1.16. The CXB and the foreground contributions were modeled as a constant over the FOV. The derived X-ray surface brightness profile of A2147 is shown in Figure 8. Using the β-model which is widely used in cases like this, we fitted the MOS2 surface brightness over a range of r= 0' – 13'. As shown by a solid line in Figure 8, the fit is acceptable with χ^2/ν= 0.68 (ν= 18-3= 15). Table 3 summarizes the obtained β-model parameters.

Table 3. Results of the single-β fit to the 0.4-8.0 keV surface brightness profile*

r_c	145".1± 45".0
β	0.50±0.14
χ^2/ν (ν= 18)	0.6*

*Fitted over a radius range from 0' to 13'

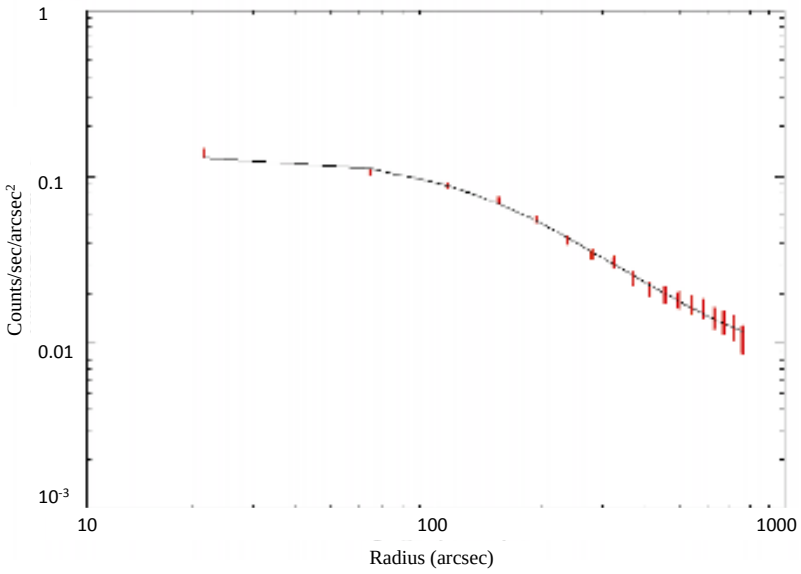

Figure 8. The 0.4-8 keV surface brightness profile of A2147 from MOS2 with statistical data plus systematical errors, fitted with a single-β model

4. Discussion

The present analysis has provided several pieces of new information about the temperature, abundance, and surface brightness distributions of XMM-Newton data of A2147. They include a significant drop in the temperature profile toward the outer radii beyond ~ 100 kpc, a loose constraint on the abundance distribution, and a successful quantification of the gravitational potential in terms of a single-β model. In this section, we will discuss these results, and compare them with those of other clusters, including Abell 1060 in particular.

4.1. Summary of results

We derived the radial temperature profile of A2147 within a radius of r= 13', (~ 600 kpc). The ICM temperature is constant at ~ 5 keV up to ~ 100 kpc, while it decreases monotonically beyond that radius, becoming ~ 3.5 keV at 600 kpc. However, its Chandra observation shows approximately

isothermal profile up to ~ 400 kpc within errors. Our results are consistent with the previous Chandra observation within the central regions as shown in Figure 9.

Then, we extracted the abundance profile for A2147 within a radius of r= 13' as shown in Figure 7. Emission-weighted abundance is 0.26 ± 0.08 solar, and best-fit values are decreasing towards outer regions. But the data are consistent, within errors, with a spatially constant abundance.

Under the assumption of the spherically symmetric distribution of the ICM, we fit the radial surface brightness profile within a radius of r= 13' with a single β-model in the energy range of 0.4-8 keV. The fitted parameters are r_{core}= 145.1 ± 45.0 arcsec= 105 ± 32.63 kpc and β= 0.5 ± 0.14. Since the surface brightness profile was described by a single β-model, the gravitational potential profile was defined by a single case length, r_c.

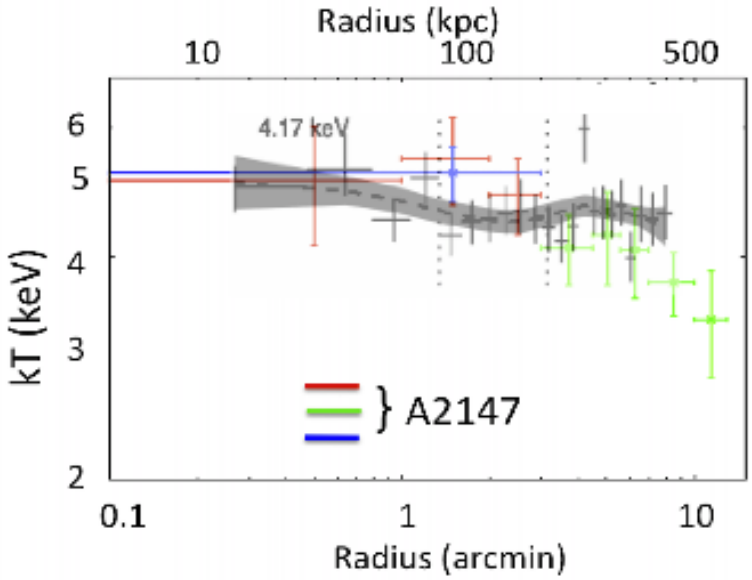

Figure 9. Comparison between A2147 and Chandra measurement

Both clusters show clear gradients for abundance profiles although both are relaxed systems without a cD galaxy.

4.2. Comparison with abundance profiles

The abundance profile of A1060 is decreasing from ~ 0.5 solar in the central region to ~ 0.2 solar in the outskirts of the cluster up to ~ 300 kpc. And, the abundance profile of A2147 is also decreasing from ~ 0.5 solar in the central region to ~ 0.1 solar in the outskirts of the cluster ~ 600 kpc.

Figure 10 shows a comparison of the abundance profiles of both clusters. Since A2147 has larger error bars, its abundance profile is consistent with being constant within errors. The figure also reveals that non-cD clusters have flatter abundance profiles than cD clusters.

4.3. Comparison with cD clusters

In addition to these, there are many differences between cD and non-cD clusters, but the origin of these differences has not been understood yet. It is well known that the temperature profile is decreasing towards the center for cD clusters within ~ 100 kpc, and there is also outward temperature decrease while the temperature profile of non-cD clusters is approximately isothermal at the center, but their outward temperature distribution has not been well known. When we compare our scaled

temperature profile with the general X-ray temperature profile for cD clusters, it is seen that cD clusters and non-cD clusters show the same temperature distribution beyond 100 kpc (Figure 11).

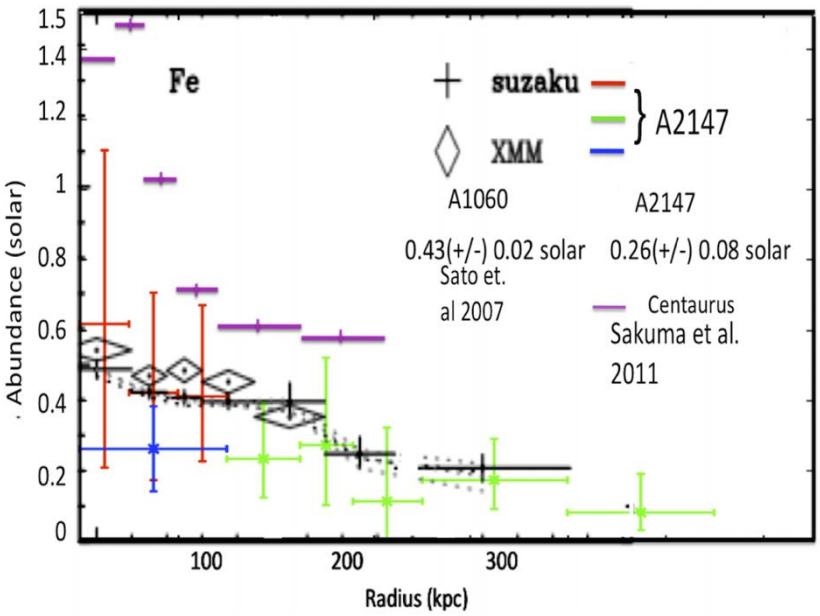

Figure 10. Comparison of A2147 abundance profile with A1060 and cD clusters

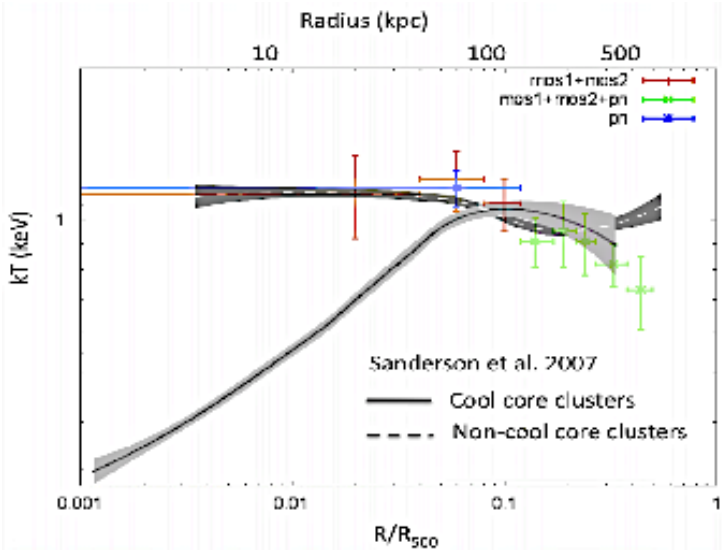

Figure 11. General X-ray temperature profile for cool-core and non-cool core clusters (Sanderson et al., 2006), comparison with A2147

4.4. Surface brightness profile

Studies show that in general, cD clusters have steeper surface brightness profile than non-cD clusters; cD clusters require double-β modeling neither single-β nor NFW model are successful. But, the surface brightness of non-cD clusters can be fitted by either double-β [13] or NFW model [18] or single-β model (as in this work). Even though both cluster types can be fitted by double-β modeling, the normalization ratio of the narrow component to a wider component is larger for cD clusters than non-cD clusters. We described the surface brightness of A2147 by a single β model with core radius of 105

kpc and β value 0.50, and its gravitational potential can be explained by a single scale length which is different from A1060.

5. Conclusion

Summing up the results presented here, let us conclude some fundamental aspects of this study. We have presented the XMM-Newton observation of the A2147 cluster of galaxies. The large effective area of XMM-Newton enables us to investigate the spatial distribution of the temperature, the metal abundance, and surface brightness in detail. We derived its temperature profile within ~ 600 kpc, it was constant at 5.2 keV in the central ~ 200 kpc, in agreement with the Chandra measurement (Sanderson et al., 2007). Beyond ~ 200 kpc, we detected mild outward temperature decrease in A2147. The overall temperature profile of A2147 was similar to that of the best-studied non-cD cluster, A1060. This temperature decreases in outer regions; observed from the two non-cD clusters, agree with those generally seen in cD clusters.

The abundance profile of A2147 confirmed that the abundance profile of non-cD clusters is inconsistent with cD clusters. The abundance profile of A2147 suggests a negative gradient similar to that of A1060, although we cannot reject a constant profile.

The gravitational potential of cD clusters usually requires two core radii because of their hierarchically nested potential shape. But, we confirmed that a single core radius of 105 kpc could describe the gravitational potential of A2147.

This scenario shows that all relaxed non-cD clusters may have similar temperature distribution in general. To confirm that studies on relaxed non-cD clusters should be supported by the data of recent satellites; observations for these specific types of clusters should be proposed for further researches.

The compliance to Research and Publication Ethics: This work was carried out by obeying research and ethics rules.

References

[1] Abell, G. O. "Clustering of galaxies", *Annual Review of Astronomy and Astrophysics*, *3*(1), 1, 1965.

[2] Jones, C., & Forman, W. "The structure of clusters of galaxies observed with Einstein", *The Astrophysical Journal*, *276*, 38-55, 1984.

[3] Fabian, A. C. "Cooling flows in clusters of galaxies", *Annual Review of Astronomy and Astrophysics*, *32*(1), 277-318, 1994.

[4] Makishima, K., Ezawa, H., Fukazawa, Y., Honda, H., Ikebe, Y., Kamae, T., ... & Takahashi, T. "X-ray probing of the central regions of clusters of galaxies", *Publications of the Astronomical Society of Japan*, *53*(3), 401-420, 2001.

[5] Kaastra, J. S., Ferrigno, C., Tamura, T., Paerels, F. B. S., Peterson, J. R., & Mittaz, J. P. D. "XMM-Newton observations of the cluster of galaxies Sérsic 159-03", *Astronomy & Astrophysics*, *365*(1), L99-L103, 2001.

[6] Tamura, T., Day, C. S., Fukazawa, Y., Hatsukade, I., Ikebe, Y., Makishima, K., ... & Yamashita, K. "Uniformity in the temperature and metallicity of the X-ray emitting gas in the Abell 1060 cluster of galaxies", *Publications of the Astronomical Society of Japan*, *48*(5), 671-677, 1996.

[7] Gu, L., Xu, H., Gu, J., Kawaharada, M., Nakazawa, K., Qin, Z., ... & Makishima, K. "Two-phase ICM in the Central Region of the Rich Cluster of Galaxies A1795: A Joint Chandra, XMM-Newton, and Suzaku View", *The Astrophysical Journal*, *749*(2), 186, 2012.

[8] Takahashi, I., Kawaharada, M., Makishima, K., Matsushita, K., Fukazawa, Y., Ikebe, Y., ... & Ota, N. "X-ray Diagnostics of Thermal Conditions of the Hot Plasmas in the Centaurus Cluster", *The Astrophysical Journal*, *701*(1), 377, 2009.

[9] Xu, H., Makishima, K., Fukazawa, Y., Ikebe, Y., Kikuchi, K. I., Ohashi, T., & Tamura, T. "Discovery of the central excess brightness in hard X-rays in the cluster of galaxies Abell 1795", *The Astrophysical Journal*, *500*(2), 738, 1998.

[10] Fitchett, Michael, and David Merritt. "Dynamics of the Hydra I galaxy cluster." *The Astrophysical Journal* 335 (1988): 18-34.

[11] Hayakawa, A., Furusho, T., Yamasaki, N. Y., Ishida, M., & Ohashi, T. "Inhomogeneity in the hot intracluster medium of Abell 1060 observed with Chandra", *Publications of the Astronomical Society of Japan*, *56*(5), 743-752, 2004.

[12] Hayakawa, A., Hoshino, A., Ishida, M., Furusho, T., Yamasaki, N. Y., & Ohashi, T. "Detailed XMM-Newton observation of the cluster of galaxies Abell 1060", *Publications of the Astronomical Society of Japan*, *58*(4), 695-702, 2006.

[13] Sato, K., Yamasaki, N. Y., Ishida, M., Ishisaki, Y., Ohashi, T., Kawahara, H., ... & Ota, N. "X-ray study of temperature and abundance profiles of the cluster of galaxies Abell 1060 with Suzaku", *Publications of the Astronomical Society of Japan*, *59*(2), 299-317, 2007.

[14] Käfer, F., Finoguenov, A., Eckert, D., Sanders, J. S., Reiprich, T. H., & Nandra, K. (2019). Toward a characterization of X-ray galaxy clusters for cosmology. *Astronomy & Astrophysics*, *628*, A43.

[15] Snowden, S. L., Mushotzky, R. F., Kuntz, K. D., & Davis, D. S. "A catalog of galaxy clusters observed by XMM-Newton", *Astronomy & Astrophysics*, *478*(2), 615-658, 2008.

[16] Kushino, A., Ishisaki, Y., Morita, U., Yamasaki, N. Y., Ishida, M., Ohashi, T., & Ueda, Y. Study of the X-ray background spectrum and its large-scale fluctuation with ASCA. *Publications of the Astronomical Society of Japan*, *54*(3), 327-352, 2002.

[17] Fujimoto, R., Mitsuda, K., McCammon, D., Takei, Y., Bauer, M., Ishisaki, Y., ... & Yamasaki, N. Y. "Evidence for solar-wind charge-exchange X-ray emission from the Earth's magnetosheath", *Publications of the Astronomical Society of Japan*, *59*(sp1), S133-S140, 2007.

[18] Tamura, T., Makishima, K., Fukazawa, Y., Ikebe, Y., & Xu, H. "X-ray measurements of the gravitational potential profile in the central region of the Abell 1060 cluster of galaxies", *The Astrophysical Journal*, *535*(2), 602, 2000.

INESEG
INTERNATIONAL ENGINEERING SCIENCE AND EDUCATION GROUP

Middle East Journal of Science

https://dergipark.org.tr/mejs

e-ISSN:2618-6136

MEJS

Research Article

ON SOME RESULTS OF WEIGHTED HÖLDER TYPE INEQUALITY ON TIME SCALES

Lütfi Akın[1]

[1]Department of Bussiness Administration, Mardin Artuklu University, 47100 Mardin, Turkey;
Corresponding author; lutfiakin@artuklu.edu.tr

Abstract: *The concept of time scales has attracted the attention of mathematicians for a quarter-century. The time scales have a very important place in mathematical analysis. Many mathematicians have worked on this subject and they have achieved good results. Inequalities and dynamic equations are at the top of these studies. Inequalities and dynamic equations contributed to the solution of many problems in various branches of science. In this article, some results of weighted Hölder type inequality are presented via* $\diamond_\alpha$*-integral.*

Keywords*: Hölder type inequality, Time scales, Integral inequalities.*

Received: April 30, 2020 Accepted: June 16, 2020

1. Introduction

Time scales have made a name in many branches of science for the last 30 years. The theory of time scales was initiated by Stefan Hilger [1] in 1988 and it was developed by many mathematicians. They have demonstrated various aspects of integral inequalities [2-32]. The most important examples of time scale studies are differential calculus and inequalities [12]. In 2014, Agarwal, O'Regan, and Saker revealed many features of dynamic inequalities in time scales. Dynamic equations and inequalities have many applications in other disciplines besides mathematics. For example; population dynamics, quantum mechanics, physical problems, wave equations, heat transfer, optical problems, and finance problems [12, 27, 29, 30].

Hölder inequalities have a very important place in harmonic analysis. Many mathematicians have achieved very important results using Hölder inequality [10, 11, 13]. The article aims to demonstrate some results of weighted Hölder's inequality in the two-dimensional case on time scale via the $\diamond_\alpha$-integral.

2. Materials and Method

Now, let's briefly give information about time scales and necessary definitions and notations for our article. The details can be followed from the studies conducted by some researchers [1-31].

$\mathbb{T}$ is a time scale ($\mathbb{T} \neq \emptyset$ and $\mathbb{T} \subset \mathbb{R}$).

Let $\sigma(t), \rho(t)$ be the forward jump operator and the backward jump operator in $\mathbb{T}$. And jump operators are defined by

$$\sigma(t) = \inf\{s \in \mathbb{T}: s > t\}, \quad \rho(t) = \sup\{s \in \mathbb{T}: s > t\}$$

for $t \in \mathbb{T}$.

If $\sigma: \mathbb{T} \to \mathbb{T}$, $\sigma(t) > t$, then t is right-scattered and if $\sigma: \mathbb{T} \to \mathbb{T}$, $\sigma(t) = t$, then t is called right-dense. If $\rho: \mathbb{T} \to \mathbb{T}$, $\rho(t) < t$, then t is left-scattered and if $\rho: \mathbb{T} \to \mathbb{T}$, $\rho(t) = t$, then t is called left-dense. Let two mappings $\mu, \vartheta: \mathbb{T} \to \mathbb{R}^+$ such that $\mu(t) = \sigma(t) - t$, $\vartheta(t) = t - \rho(t)$ are called graininess mappings.

Let $g: \mathbb{T} \to \mathbb{R}$ and $g^\sigma: \mathbb{T} \to \mathbb{R}$ by $g^\sigma(t) = g(\sigma(t))$ for $\forall t \in \mathbb{T}$, i.e., $g^\sigma = g \circ \sigma$. And let $g: \mathbb{T} \to \mathbb{R}$ and $g^\rho: \mathbb{T} \to \mathbb{R}$ by $g^\rho(t) = g(\rho(t))$ for $\forall t \in \mathbb{T}$, i.e., $g^\rho = g \circ \rho$.

The generalized derivative $g^\Delta(t)$ of $g: \mathbb{T} \to \mathbb{R}$, becomes $g^\Delta(t) = g'(t)$ when $\mathbb{T} = \mathbb{R}$. And if $\mathbb{T} = \mathbb{Z}$, then $g^\Delta(t)$ reduces to $g^\Delta(t) = \Delta g(t)$.

Definition 2.1. If $G: \mathbb{T} \to \mathbb{R}$ is called a Δ-antiderivative of $g: \mathbb{T} \to \mathbb{R}$, then we define

$$\int_s^t g(\delta)\Delta\delta = G(t) - G(s),$$

for $\forall s, t \in \mathbb{T}$. [12]

Definition 2.2. Let $h: \mathbb{T}_k \to \mathbb{R}$ is called ∇-differentiable at $t \in \mathbb{T}_k$. If $\varepsilon > 0$, then there exists a neighborhood V of t such that

$$\left|h\big(\rho(t)\big) - h(s) - h^\nabla(t)(\rho(t) - s)\right| \leq \varepsilon|\rho(t) - s|,$$

for $\forall s \in V$. [14]

Definition 2.3. Let $H: \mathbb{T} \to \mathbb{R}$ is called a ∇-antiderivative of $h: \mathbb{T} \to \mathbb{R}$, then we define

$$\int_s^t h(\delta)\nabla\delta = H(t) - H(s),$$

for $s, t \in \mathbb{T}$. [14]

Let $f(t)$ be differentiable on $\mathbb{T}$ for $\alpha, t \in \mathbb{T}$. Then, we define $f^{\diamond\alpha}(t)$ by

$$f^{\diamond\alpha}(t) = \alpha f^\Delta(t) + (1 - \alpha)f^\nabla(t)$$

for $0 \leq \alpha \leq 1$. [14]

Proposition 2.4. If we get $f, h: \mathbb{T} \to \mathbb{R}$, $\diamond_\alpha$-differentiable for $\alpha, t \in \mathbb{T}$, [15] then

(i) $f + h: \mathbb{T} \to \mathbb{R}$ is $\diamond_\alpha$-differentiable for $t \in \mathbb{T}$ with

$$(f + h)^{\diamond\alpha}(t) = f^{\diamond\alpha}(t) + h^{\diamond\alpha}(t).$$

(ii) Let $k \in \mathbb{R}$, $kf: \mathbb{T} \to \mathbb{R}$ is $\diamond_\alpha$-differentiable for $\alpha, t \in \mathbb{T}$ with

$$(kf)^{\diamond\alpha}(t) = kf^{\diamond\alpha}(t).$$

(iii) $fh: \mathbb{T} \to \mathbb{R}$ is $\diamond_\alpha$-differentiable for $\alpha, t \in \mathbb{T}$ with

$$(fh)^{\diamond\alpha}(t) = f^{\diamond\alpha}(t).h(t) + \alpha f^{\sigma}(t)h^{\Delta}(t) + (1-\alpha)f^{\rho}(t)h^{\nabla}(t).$$

Definition 2.5. If we get $\alpha, b, t \in \mathbb{T}$ and $f: \mathbb{T} \to \mathbb{R}$, [15] then

$$\int_b^t f(\tau) \diamond_\alpha \gamma = \alpha \int_b^t f(\gamma)\Delta\gamma + (1-\alpha)\int_b^t f(\gamma)\nabla\gamma$$

for $0 \le \alpha \le 1$.

Proposition 2.6. Let $u, v, \alpha, t \in \mathbb{T}$, $c \in \mathbb{R}$ and if $f(\gamma)$, $g(\gamma)$ are $\diamond_\alpha$-integrable on $[u, v]_{\mathbb{T}}$, then the following statements are valid. [15]

(i) $\int_u^t [f(\gamma) + g(\gamma)] \diamond_\alpha \gamma = \int_u^t f(\gamma) \diamond_\alpha \gamma + \int_u^t g(\gamma) \diamond_\alpha \gamma$,
(ii) $\int_u^t cf(\gamma) \diamond_\alpha \gamma = c\int_u^t f(\gamma) \diamond_\alpha \gamma$,
(iii) $\int_u^t f(\gamma) \diamond_\alpha \gamma = -\int_t^u f(\gamma) \diamond_\alpha \gamma$,
(iv) $\int_u^t f(\gamma) \diamond_\alpha \gamma = \int_u^v f(\gamma) \diamond_\alpha \gamma + \int_v^t f(\gamma) \diamond_\alpha \gamma$,
(v) $\int_u^u f(\gamma) \diamond_\alpha \gamma = 0$.

Lemma 2.7. Let $u, v, \alpha, t \in \mathbb{T}$ with $u < v$. Suppose that $h(\gamma)$ and $g(\gamma)$ are $\diamond_\alpha$-integrable on $[u, v]_{\mathbb{T}}$, then we have [15]

(i) If $h(\gamma) \ge 0$ for $\forall\gamma \in [u, v]_{\mathbb{T}}$, then $\int_u^v h(\gamma) \diamond_\alpha \gamma \ge 0$.
(ii) If $h(\gamma) \le g(\gamma)$ for $\forall\gamma \in [u, v]_{\mathbb{T}}$, then $\int_u^v h(\gamma) \diamond_\alpha \gamma \le \int_u^v g(\gamma) \diamond_\alpha \gamma$.
(iii) If $h(\gamma) \ge 0$ for $\forall\gamma \in [u, v]_{\mathbb{T}}$, then $h(\gamma) = 0$ iff $\int_u^v h(\gamma) \diamond_\alpha \gamma = 0$.

Lemma 2.8. Let h, g be ∇-differentiable two positive functions [31]. For h, g satisfying $g^q l \le h^p \le g^q L$ on the $[a, b]$, with $1/p + 1/q = 1$ and $p, q > 1$, we have

$$(l)^{1/pq}\left(\int_a^b h(s)^p \nabla s\right)^{1/p}\left(\int_a^b g(s)^q \nabla s\right)^{1/q} \le (L)^{1/pq}\int_a^b h(s)g(s)\nabla s.$$

Theorem 2.9. If h is $\diamond_\alpha$-integrable on an interval $I = [a, b]$, then $|h|$ is $\diamond_\alpha$-integrable on I that is [31]

$$\left|\int_I h(s) \diamond_\alpha s\right| \le \int_I |h(s)| \diamond_\alpha s.$$

3. Results

Theorem 3.1. Let two mappings $h, g \in C_{rd}$ and $h, g: [a, b] \times [a, b] \to \mathbb{R}$. $\theta(\gamma, \tau), \vartheta(v, \tau) > 0$ weight functions and $\diamond_\alpha$-integrable functions for $a, b \in \mathbb{T}$, we have

$$\int_a^b \int_a^b |h(\gamma,\tau)\theta(\gamma,\tau)g(\gamma,\tau)\vartheta(\gamma,\tau)| \diamond_\alpha \gamma \diamond_\alpha \tau$$

$$\leq \left(\int_a^b \int_a^b |h(\gamma,\tau)\theta(\gamma,\tau)|^p \diamond_\alpha \gamma \diamond_\alpha \tau \right)^{\frac{1}{p}} \left(\int_a^b \int_a^b |g(\gamma,\tau)\vartheta(\gamma,\tau)|^q \diamond_\alpha \gamma \diamond_\alpha \tau \right)^{\frac{1}{q}}$$

where $p > 1,\ q > 1$.

Proof. If $u, v \geq 0$ $(u, v \in \mathbb{R})$ with $1/p + 1/q = 1$ $(p, q > 1)$, then

$$qu^{\frac{1}{q}} + pv^{\frac{1}{p}} \geq pq \tag{1}$$

holds. Assume that

$$\left(\int_a^b \int_a^b |h(\gamma,\tau)\theta(\gamma,\tau)|^p \diamond_\alpha \gamma \diamond_\alpha \tau \right) \left(\int_a^b \int_a^b |g(\gamma,\tau)\vartheta(\gamma,\tau)|^q \diamond_\alpha \gamma \diamond_\alpha \tau \right) \neq 0.$$

and $u(\gamma,\tau), v(\gamma,\tau) \in C_{rd}(\mathbb{R})$ with

$$u(\gamma,\tau) = \frac{|h(\gamma,\tau)\theta(\gamma,\tau)|^p}{\int_a^b \int_a^b |h(\delta_1,\delta_2)\theta(\delta_1,\delta_2)|^p \diamond_\alpha \delta_1 \diamond_\alpha \delta_2},$$

$$v(\gamma,\tau) = \frac{|g(\gamma,\tau)\vartheta(\gamma,\tau)|^q}{\int_a^b \int_a^b |g(\delta_1,\delta_2)\vartheta(\delta_1,\delta_2)|^q \diamond_\alpha \delta_1 \diamond_\alpha \delta_2}.$$

If we apply (1) to functions $u(\gamma,\tau)$ and $v(\gamma,\tau)$ and take integrals from a to b, we get directly Hölder inequalities

$$\int_a^b \int_a^b \frac{|h(\gamma,\tau)\theta(\gamma,\tau)|^p}{\int_a^b \int_a^b |h(\delta_1,\delta_2)\theta(\delta_1,\delta_2)|^p \diamond_\alpha \delta_1 \diamond_\alpha \delta_2} \cdot \frac{|g(\gamma,\tau)\vartheta(\gamma,\tau)|^q}{\int_a^b \int_a^b |g(\delta_1,\delta_2)\vartheta(\delta_1,\delta_2)|^q \diamond_\alpha \delta_1 \diamond_\alpha \delta_2} \diamond_\alpha \gamma \diamond_\alpha \tau$$

$$= \int_a^b \int_a^b u(\gamma,\tau)^{\frac{1}{p}} v(\gamma,\tau)^{\frac{1}{q}} \diamond_\alpha \gamma \diamond_\alpha \tau \leq \int_a^b \int_a^b \left[\frac{u(\gamma,\tau)}{p} + \frac{v(\gamma,\tau)}{q} \right] \diamond_\alpha \gamma \diamond_\alpha \tau$$

$$= \frac{1}{p} \int_a^b \int_a^b \frac{|h(\gamma,\tau)\theta(\gamma,\tau)|^p}{\int_a^b \int_a^b |h(\delta_1,\delta_2)\theta(\delta_1,\delta_2)|^p \diamond_\alpha \delta_1 \diamond_\alpha \delta_2} \diamond_\alpha \gamma \diamond_\alpha \tau$$

$$+ \frac{1}{q} \int_a^b \int_a^b \frac{|g(\gamma,\tau)\vartheta(\gamma,\tau)|^q}{\int_a^b \int_a^b |g(\delta_1,\delta_2)\vartheta(\delta_1,\delta_2)|^q \diamond_\alpha \delta_1 \diamond_\alpha \delta_2} \diamond_\alpha \gamma \diamond_\alpha \tau$$

$$= \frac{1}{p} + \frac{1}{q} = 1.$$

Theorem 3.2. Let $\theta(\gamma,\tau),\vartheta(\gamma,\tau)>0$ be weight functions via $\diamond_\alpha$-integrable. If $M(\gamma,\tau),h(\gamma),g(\tau),\mu(\gamma),\sigma(\tau)$ be non-negative functions with $1/p+1/q=1$ $(p,q>1)$ via $\diamond_\alpha$-integrable, then the following (2) and (3) inequalities are equivalent

$$\int_a^b\int_a^b M(\gamma,\tau)h(\gamma)\theta(\gamma,\tau)g(\tau)\vartheta(\gamma,\tau)\diamond_\alpha\gamma\diamond_\alpha\tau$$

$$\leq\left(\int_a^b \mu(\gamma)^p K(\gamma)(h(\gamma)\theta(\gamma))^p\diamond_\alpha\gamma\right)^{\frac{1}{p}}\left(\int_a^b \sigma(\tau)^q D(\tau)(g(\tau)\vartheta(\tau))^q\diamond_\alpha\tau\right)^{\frac{1}{q}} \tag{2}$$

and

$$\int_a^b \sigma(\tau)^{-p}D(\tau)^{1-p}\left(\int_a^b M(\gamma,\tau)h(\gamma)\theta(\gamma)\diamond_\alpha\gamma\right)^p\diamond_\alpha y\leq\int_a^b\mu(\gamma)^pK(\gamma)(h(\gamma)\theta(\gamma))^p\diamond_\alpha\gamma \tag{3}$$

where $K(\gamma)=\int_a^b\frac{M(\gamma,\tau)}{\sigma(y)^p}\diamond_\alpha\tau$ and $D(y)=\int_a^b\frac{M(\gamma,\tau)}{\mu(\gamma)^q}\diamond_\alpha\gamma$.

Proof. Let's consider the equation below

$$\int_a^b\int_a^b M(\gamma,\tau)h(\gamma)\theta(\gamma,\tau)g(\tau)\vartheta(\gamma,\tau)\diamond_\alpha\gamma\diamond_\alpha\tau$$

$$=\int_a^b\int_a^b M(\gamma,\tau)h(\gamma)\theta(\gamma,\tau)\frac{\mu(\gamma)}{\sigma(\tau)}g(\tau)\vartheta(\gamma,\tau)\frac{\sigma(\tau)}{\mu(\gamma)}\diamond_\alpha\gamma\diamond_\alpha\tau. \tag{4}$$

Now, applying the Hölder inequality to (4), we get

$$\int_a^b\int_a^b M(\gamma,\tau)h(\gamma)g(\tau)\diamond_\alpha\gamma\diamond_\alpha\tau$$

$$\leq\left(\int_a^b\mu(\gamma)^pK(\gamma)(h(\gamma)\theta(\gamma))^p\diamond_\alpha\gamma\right)^{\frac{1}{p}}\left(\int_a^b\sigma(\tau)^qD(\tau)(g(\tau)\vartheta(\tau))^q\diamond_\alpha\tau\right)^{\frac{1}{q}}.$$

Assume that the inequality (2) holds. If

$$g(\tau)=\sigma(\tau)^{-p}D(\tau)^{1-p}\left(\int_a^b M(\gamma,\tau)h(\gamma)\theta(\gamma)\diamond_\alpha\gamma\right)^{p-1}$$

and using (2), we obtain

$$\int_a^b\sigma(\tau)^{-p}D(\tau)^{1-p}\left(\int_a^b M(\gamma,\tau)h(\gamma)\theta(\gamma)\diamond_\alpha\gamma\right)^p\diamond_\alpha\tau$$

$$= \int_a^b \int_a^b M(\gamma,\tau)h(\gamma)\theta(\gamma)g(y) \diamond_\alpha \gamma \diamond_\alpha \tau$$

$$\leq \left(\int_a^b \mu(\gamma)^p K(\gamma)(h(\gamma)\theta(\gamma))^p \diamond_\alpha \gamma \right)^{\frac{1}{p}} \left(\int_a^b \sigma(\tau)^q D(\tau)\big(g(\tau)\vartheta(\tau)\big)^q \diamond_\alpha \tau \right)^{\frac{1}{q}}$$

$$= \left(\int_a^b \mu(\gamma)^p K(\gamma)(h(\gamma)\theta(\gamma))^p \diamond_\alpha \gamma \right)^{\frac{1}{p}} \left(\int_a^b \sigma(\tau)^{-p} D(\tau)^{1-p} \left(\int_a^b M(\gamma,\tau)h(\gamma)\theta(\gamma) \diamond_\alpha \gamma \right)^p \diamond_\alpha \tau \right)^{\frac{1}{q}}.$$

Now, applying Hölder's inequality, we obtain

$$\int_a^b \int_a^b M(\gamma,\tau)h(\gamma)\theta(\gamma)g(\tau)\vartheta(\tau) \diamond_\alpha \gamma \diamond_\alpha \tau$$

$$= \int_a^b \left(\sigma(\tau)^{-1} D\tau^{\frac{-1}{q}} \int_a^b M(\gamma,\tau)h(\gamma)\theta(\gamma) \diamond_\alpha \gamma \right) \sigma(\tau)D(\tau)^{\frac{1}{q}} g(\tau)\vartheta(\tau) \diamond_\alpha \tau$$

$$\leq \left(\int_a^b \sigma(\tau)^{-p} D(\tau)^{1-p} \left(\int_a^b M(\gamma,\tau)h(\gamma)\theta(\gamma) \diamond_\alpha \gamma \right)^p \diamond_\alpha \tau \right)^{\frac{1}{p}} \left(\int_a^b \sigma(\tau)^q D(\tau)(g(\tau)\vartheta(\tau))^q \diamond_\alpha \tau \right)^{\frac{1}{q}}$$

$$\leq \left(\int_a^b \mu(\gamma)^p K(\gamma)(h(\gamma)\theta(\gamma))^p \diamond_\alpha \gamma \right)^{\frac{1}{p}} \left(\int_a^b \sigma(\tau)^q D(\tau)(g(\tau)\vartheta(\tau))^q \diamond_\alpha \tau \right)^{\frac{1}{q}}.$$

4. Discussion

Integration in time scales helps us to achieve many nonlinear integral equations using different inequalities and equations. Many authors have obtained many inequalities and integral equations using various methods [1-32]. The method we use in this article can be applied to other inequalities and equations provided that they meet the requirements. We focused on the concept of weight in inequalities and dynamic equations. In addition, we have obtained some results by using Hölder type inequality in time scales inspired by these studies.

The compliance to Research and Publication Ethics: This work was carried out by obeying research and ethics rules.

References

[1] Hilger, S. Ein Maßkettenkalkül mit Anwendung auf Zentrmsmannigfaltingkeiten, Ph.D. Thesis, Univarsi. Würzburg, 1988.

[2] Agarwal, R.P., Bohner, M., Peterson, A., "Inequalities on time scales: A survey", *Math. Inequal. Appl.*, 4, 535-555, 2001.

[3] Akin-Bohner, A., Bohner, M., Akin, F., "Pachpatte inequalities on time scales", *Journal of Inequalities in Pure and Applied Mathematics*, 6(1), 1-23, 2005.

[4] Li, W.N., "Nonlinear Integral Inequalities in Two Independent Variables on Time Scales". *Adv Differ Equ.*Vol. 2011, 1-11, 2011 doi:10.1155/2011/283926

[5] Anastassiou, G.A., "Principles of delta fractional calculus on time scales and inequalities", *Mathematical and Computer Modelling*, 52, 556-566, 2010.

[6] Wong, F.-H., Yeh, C.-C.,Yu, S.L.,Hong, C.-H., "Young's inequality and related results on time scales," *Appl. Math. Lett*. 18, 983–988, 2005.

[7] Wong, F.-H., Yeh, C.-C., Lian, W.-C., "An extension of Jensen's inequality on time scales," *Adv. Dynam. Syst. Appl*., 1(1), 113–120, 2006.

[8] Kuang, J., Applied inequalities, Shandong Science Press, Jinan, 2003.

[9] Uçar, D., Hatipoğlu, V.F., Akincali, A., "Fractional Integral Inequalıties on Tıme Scales." *Open J. Math. Sci*., 2(1), 361-370, 2018.

[10] Özkan, U.M., Sarikaya, M.Z., Yildirim, H., "Extensions of certain integral inequalities on time scales", *Appl. Math. Lett*. 21, 993–1000, 2008.

[11] Tian, J.-F., Ha, M.-H., "Extensions of Hölder-type inequalities on time scales and their applications*," J. Nonlinear Sci. Appl*., 10, 937–953, 2017.

[12] Kac, V., Cheung, P., Quantum Calculus. Universitext Springer, New York 2002.

[13] Yang, W.-G., "A functional generalization of diamond-α integral Hölder's inequality on time scales," *Appl. Math. Lett*, 23, 1208–1212, 2010.

[14] Bohner, M., Peterson, A., *Dynamic equations on time scales, an introduction with applications,* Birkhauser, Boston, 2001.

[15] Sheng, Q., Fadag, M., Henderson, J., Davis, J.M., "An exploration of combined dynamic derivatives on time scales and their applications," *Nonlinear Anal. Real World Appl*. 7, 395–413, 2006.

[16] Qi, F., "Several integral inequalities." *RGMIA Res. Rep. Coll*., 2(7), 1039–1042, 1999.

[17] Qi, F., "Several integral inequalities." *J. Inequal. Pure Appl. Math*, 1(2), 1-3, 2000 http://www.emis.de/journals/JIPAM/article113.html,

[18] Hilger, S., "Analysis on measure chains-a unified approach to continuous and discrete calculus" *Results Math.*, 18, 18–56, 1990.

[19] Agarwal, R.P., O'Regan, D., Saker, S.H., *Dynamic Inequalities on Time Scales*, Springer, Heidelberg, New York, Drodrechet, London 2014.

[20] Li, W.N., "Nonlinear Integral Inequalities in Two Independent Variables on Time Scales" *Adv Differ Equ*.,Vol 2011, 1-11, 2011ş doi:10.1155/2011/283926

[21] Bohner, M., Agarwal, R.P., "Basic calculus on time scales and some of its applications" *Resultate der Mathematic*, 35, 3-22. 1999.

[22] Bohner, M., Guseinov, G.S., "Multiple Lebesgue integration on time scales." *Adv. Differ. Equ*., 2006, 1–14, 2006. DOI 10.1155/ADE/2006/26391

[23] Chen, G., Wei, C., "A functional generalization of diamond-α integral Dresher's inequality on time scales" *Adv. Differ. Equ*., 3(24), 1-7, 2014 http://www.advancesindifferenceequations.com/content/2014/1/324,

[24] Yin, L., Qi, F., "Some Integral Inequalities on Time Scales," *Results in Math*., 64, 371–381. 2013. DOI: 10.1007/s00025-013-0320-z.

[25] Qi, F., Li, A.-J., Zhao, W.-Z., Niu, D.-W., Cao, J., "Extensions of several integral inequalities" *J. Inequal.Pure Appl. Math*., 7(3), 1-6, 2006. http://www.emis.de/journals/JIPAM/article706.html,

[26] Spedding, V., "Taming nature's numbers," *New Scientist*, 19, 28–31, 2003.

[27] Tisdell, C.C., Zaidi, A., "Basic qualitative and quantitative results for solutions to nonlinear dynamic equations on time scales with an application to economic modelling" *Nonlinear Anal*., 68, 3504–3524, 2008.

[28] Bohner, M., Heim, J., Liu, A., "Qualitative analysis of Solow model on time scales" *J. Concrete Appl. Math*., 13, 183–197, 2015.

[29] Brigo, D., Mercurio, F., "Discrete time vs continuous time stock-price dynamics and implications for option pricing" *Finance Stochast*., 4, 147–159, 2000.

[30] Seadawy, A.R., Iqbal, M., Lu, D., "Nonlinear wave solutions of the Kudryashov–Sinelshchikov dynamical equation in mixtures liquid-gas bubbles under the consideration of heat transfer and viscosity" *Journal of Taibah University for Science*, 13(1), 1060-1072, 2019. DOI: 10.1080/16583655.2019.1680170.

[31] Tuna, A., Kutukcu, S., "Some integral inequalities on time scales" *Applied Mathematics and Mechanics* (English Edition), 29(1), 23-28, 2008.

[32] Krnıc, M., Pecarıc, J., "General Hilbert's an Hardy's inequality" *J. Math Ineq and Appl*, 8, 29–51, 2005.

INESEG
INTERNATIONAL ENGINEERING SCIENCE AND EDUCATION GROUP

Middle East Journal of Science

https://dergipark.org.tr/mejs

e-ISSN:2618-6136

MEJS

Research Article

THE EFFECTS OF THE MN^{2+} IONS ON THE MORPHOLOGICAL PROPERTIES OF ZINC OXIDE THIN FILMS

Cihat Aydin*[1] ***Ayhan Orhan***[2]

[1]Department of Metallurgy and Materials Engineering, Engineering Faculty, Mersin University, Mersin, Turkey

[2]Department of Metallurgy and Materials Engineering, Faculty of Technology, Firat University, Elazig, Turkey
* Corresponding author; cihataydin@mersin.edu.tr

Abstract: *The nanocrystalline ZnO thin films were successfully prepared via the sol-gel spin coating method for the different atomic ratios Mn doping (0.1%, 0.5%, 1%, 2%, 5%). The detailed surface analysis of samples was performed by Atomic Force Microscopy (AFM). The AFM results indicate that the ZnO films have nanostructure. The morphological characteristics of films show that Mn2+ ions are included in the crystal lattice of ZnO without changing the structure. The influence of Mn doping on film growth has resulted in an increase in fiber size and roughness. The fiber size values of the films were found to vary from 0.898 µm to 2.960 µm with Mn doping. The study revealed the possibility with Mn doping of controlling, optimizing and improving the morphology in ZnO thin-film production.*

Keywords*: Mn-doped ZnO, Morphological analysis, Atomic force Microscopy, Microfiber, Roughness*

Received: March 28, 2020 Accepted: May 05, 2020

1. Introduction

As a multifunctional material, ZnO has been known for a long time and has a wide range of uses due to its remarkable properties [1, 2]. Therefore, ZnO is a suitable material for electronic and optical devices [3]. Furthermore, ZnO offers unique photocatalytic properties [4].

The modification of the superior properties of zinc oxide by doping has been extensively investigated, but studies are still ongoing [5]. Nonetheless, the physical, optical, morphological, and electrical characteristics of ZnO nanostructures can be improved by the doping of some transition metal ions such as Cr, Mn, Fe, Co, and Ni [6, 7]. The doped metal oxide, incorporated into ZnO nanostructures, affects its bandgap, electrical and optical characteristics [8]. The contribution of metal oxides or transition metals leads to an increase in surface imperfections, which are the cause of electrical and optical conductivity [9]. These transition metal ions, especially Mn^{2+}-ions, are important because they are optically active and provide localized spins that interact with the spin of electrons/gaps in the host lattice [10]. Furthermore, the fact that the ionic radius of Mn^{2+} (0.066 nm) is close to the ionic radius of Zn^{2+} (0.060 nm) is one of the most important reasons for choosing Mn^{2+}-ions as a dopant [11].

Various film parameters such as thickness and homogeneity must be accurately controlled in the production of thin films to be used in different application areas [12]. The sol-gel spin coating technique offers advantages, including better stoichiometry control [13], lower process temperature [14], better homogeneity [15], low cost, the use of high purity starting materials [16], and the easy coating of large substrates [17, 18]. For these reasons, this method is one of the simplest and most effective methods of producing thin films in a controlled manner [19-21]. It is possible to use pure and Mn-doped ZnO nanostructures in optoelectronic devices that have great importance due to their optical properties. Numerous studies in this field have been conducted mostly on magnetic characteristics of Mn-doped nanostructured ZnO thin films. However, there is no study based on morphological properties in the literature.

In the present research, nanostructured doped and pure ZnO films were deposited on commercial glass substrates by employing the spin coating technique. The main objective is to examine the effects of Mn-concentration on the microstructure and optoelectrical properties of ZnO in detail. Despite the fact that a number of structural, morphological, magnetic, and optical characteristics of Mn-doped ZnO films produced by the spin coating technique have been reported in various studies, based on the surface morphology have not been encountered much in the current literature. Moreover, only a few articles report on the nonlinear optical approach of this layer based on the Mn-doped ZnO layers.

2. Materials and Methods

2.1. Materials

All chemicals used in the processes are provided by Sigma-Aldrich. 2-methoxy ethanol (CH3OCH2CH2OH) (purity 99.8%) as the solvent, and monoethanolamine (MEA) (purity ≥ 99.0%) as the stabilizer, Manganese(II) acetate tetrahydrate ((CH3CO2)2Mn.4H2O) (purity ≥ 99%) as the dopant source and zinc acetate dihydrate (Zn(CH3COO)2.2H2O) (purity 99.9%) was utilized as the starting material, and their analytical purity was maintained.

2.2. The preparation process of gels

Zinc acetate was doped with Manganese (II) acetate tetrahydrate at different atomic ratios (0, 0.1, 0.5, 1, 2, and 5 %) to form the sol-gel solutions of ZnO that contained Mn- at various atomic ratios. The solutions, measured as 1 M and 10 ml, were placed in a test tube containing 2-methoxy ethanol as solvent. These solutions were then stirred at room temperature using a magnetic stirrer (5 minutes at 1000 rpm) and an ultrasonic stirrer (5 minutes). This stirring process was repeated under identical conditions after adding the dopant source. After the doping, the stabilizer (monoethanolamine) was added and stirred under the same conditions. Finally, the mixture was stirred for 60 min at 60 C with a magnetic stirrer in order to obtain a homogeneous sol- from the solution,

2.3. Deposition of the pure and Mn-doped ZnO nanolayers

Microscope glass was used as a substrate to grow the obtained Mn: ZnO gels as a thin film layer. The microscope glasses were cleaned ultrasonically with acetone, ethyl alcohol and de-ionized water for 10 minutes, respectively. After cleaning, glasses were completely dried by using nitrogen gas. The growth of thin films on glass substrates was carried out by a spin coater (1000 rpm, 30 seconds). The above-mentioned procedure was repeated 5 times in order to obtain a homogeneous surface. For drying,

the substrates were held on a heater pre-set to 200 °C for 5 min. In the last step, the acquired films were heat-treated at a temperature of 500 °C for 60 min. Care was taken to prepare thin films under the same conditions for all the doping ratios.

2.4. Characterization techniques

For the purpose of examining the topographic characteristics of Mn: ZnO thin films, 2D and 3D-micrographs of the surfaces were obtained by a PARK SYSTEM XE-100E Atomic Force Microscope. The structural characteristics of the formative phases of the nanolayers were examined. In order to capture images from the nanolayers surface, a suitable cantilever and the non-contact mode was utilized. After the 40 μm x 40 μm and 5 μm x 5 μm images of Mn: ZnO thin films were obtained, the detailed morphological analysis of the scanned regions was performed on each sample surface.

3. Results and Discussion

3.1. Detailed morphological analysis of nanostructured Mn: ZnO thin films

Figs. 1(a-f) shows the 2D/3D AFM micrographs obtained at different magnifications (40 μm x 40 μm and 5 μm x 5 μm) of pure and Mn-doped ZnO film samples. From the obtained micrographs, it is determined that the surface morphology of Mn-doped ZnO films is formed in the form of nanofiber by the combination of nano-sized granules and in the form of microfiber by the combination of these nanofibers. These microfibers are uniformly dispersed, even though dense and irregular on the film surface. The size and shape of fibers change according to Mn-concentrations. As the Mn ratio increases, it is determined that the size of the microfibers formed increases in parallel with the increasing grain size. The reason for the mentioned alteration in fiber dimensions is Mn-atoms forming the intermediate position in ZnO [22]. By using AFM images, the surface roughness values (R_q) of thin films were computed to be 61.053, 68.384, 71.534, 123.955, 169.251, and 189.985 nm for 0, 0.1, 0.5, 1, 2, and 5% of Mn-doped ZnO samples, respectively. A linear representation of the surface roughness and cross-sectional analysis of the samples is given in Fig. 2 (a-f).

The sample with the lowest R_q is pure ZnO. The increase in the size of the microfibres also increased the surface roughness value. The lower roughness value of the pure ZnO sample showed a more homogeneous distribution of small grains on the surface in terms of surface morphology. 2D-AFM images obtained at high resolution, high magnifications and line profiles of the fibers forming the morphology of the samples are shown in Figs. 3 (a-f).

The red markers in the line profiles indicate the microfiber, while the blue and green markers indicate the nanofibers that make up this microfiber. From the AFM micrographs and line profiles in Fig. 3 (a-f), it is observed that microfibers are formed by the combined growth of multiple nanofibers with the help of doping. With the addition of Mn-doping to the ZnO matrix, the structure of the fiber (Fig. 3-a) formed by nanogranules changes. These nanogranules are shaped in the form of nanofibers, and then they were changed together to form microfibers.

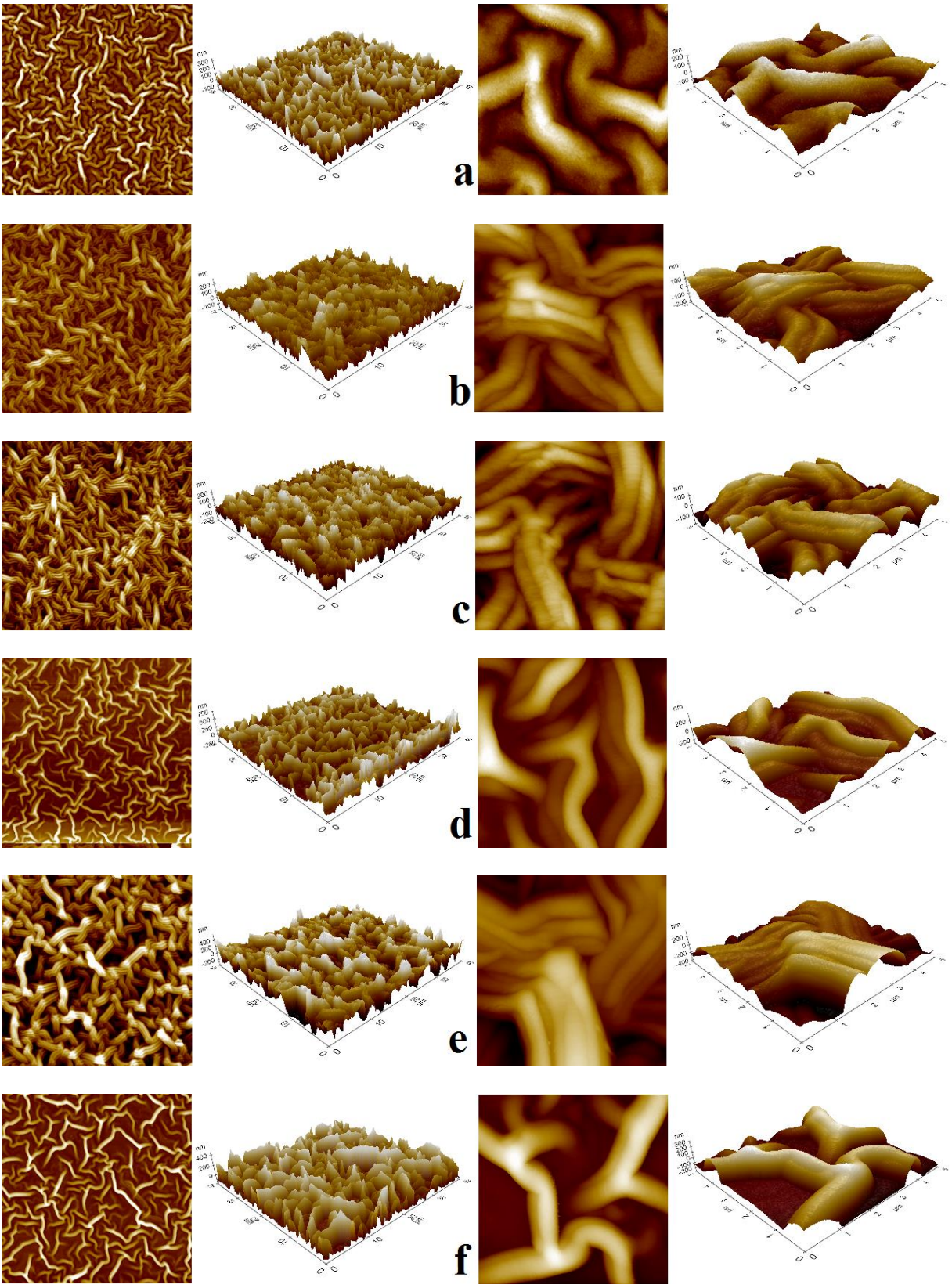

Fig. 1. AFM Micrographs of undoped and Mn-doped ZnO nanocrystals.
a) ZnO, **b)** 0.1 % Mn, **c)** 0.5 % Mn, **d)** 1 % Mn, **e)** 2 % Mn and **f)** 5 % Mn
Left (40 µm x 40 µm) 2D/3D –view, Right (5 µm x 5 µm) 2D/3D –view

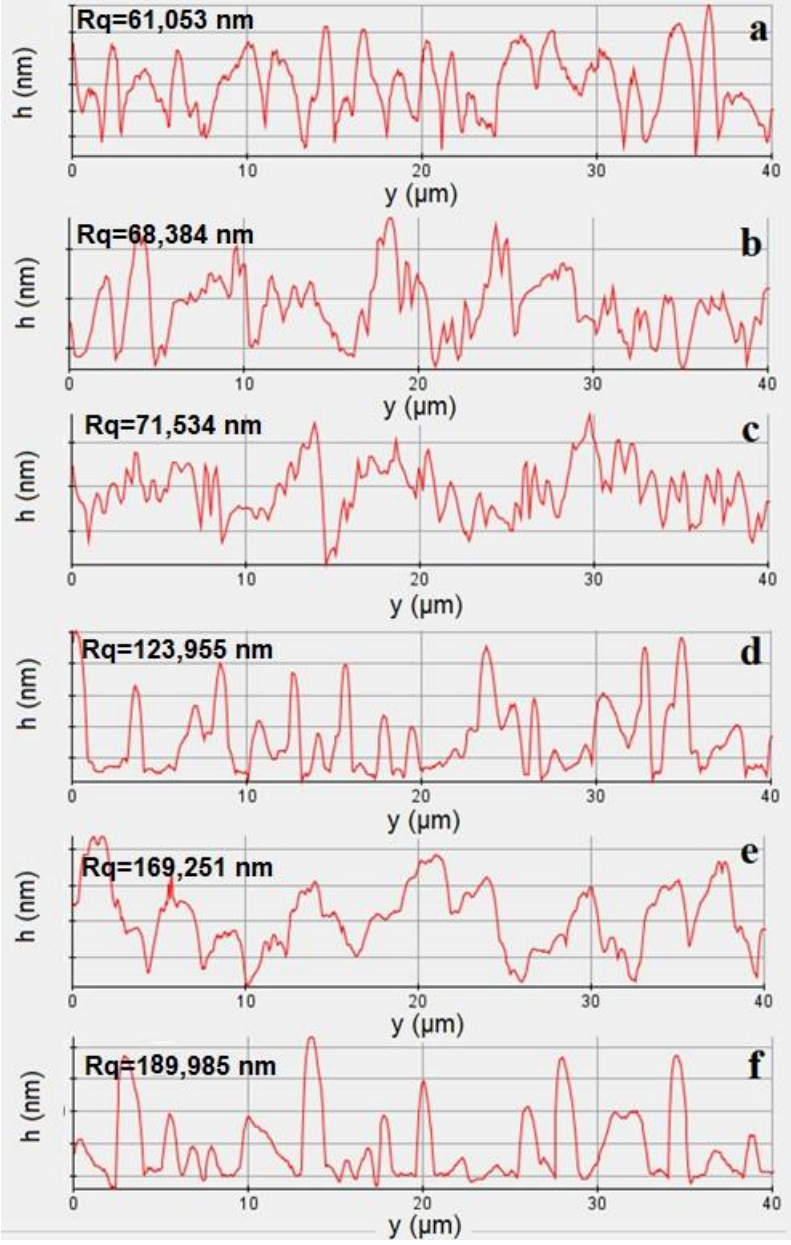

Fig. 2. AFM section analysis of Mn-doped ZnO thin films.
a) ZnO, **b)** 0.1 % Mn, **c)** 0.5 % Mn, **d)** 1 % Mn, **e)** 2 % Mn and **f)** 5 % Mn

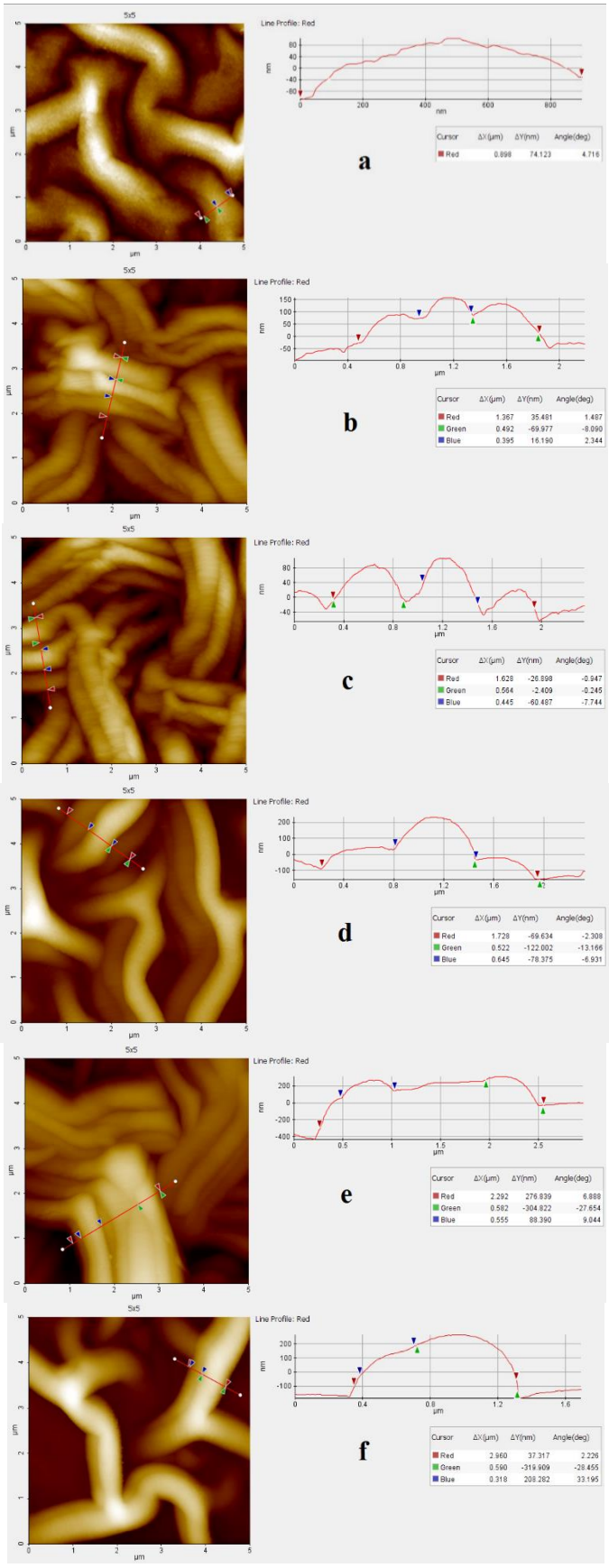

Fig. 3. AFM image and line profiles of ZnO fibers in samples

a) ZnO, **b)** 0.1 % Mn, **c)** 0.5 % Mn, **d)** 1 % Mn, **e)** 2 % Mn and **f)** 5 % Mn

The total thickness of the fibers of the samples was calculated to be 0.898, 1.367, 1.628, 1.728, 2.292, and 2.960 µm for 0, 0.1, 0.5, 1, 2, and 5% Mn-doped ZnO film samples, respectively. The variation in surface roughness and fiber size depending on manganese content is given in Fig. 4.

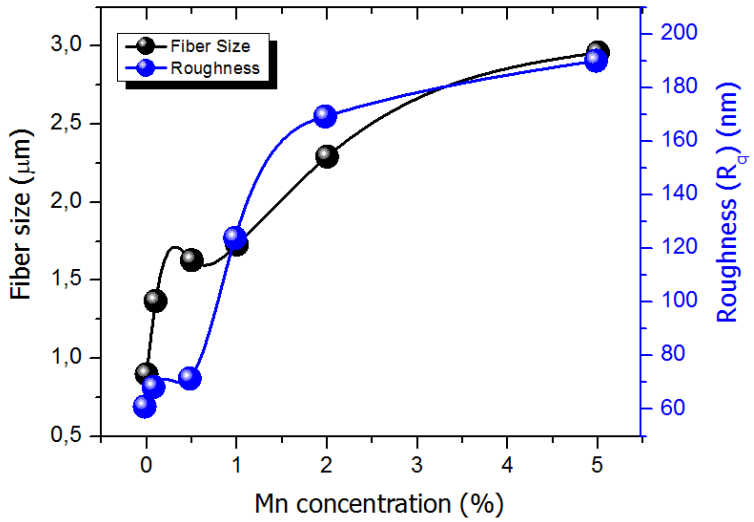

Fig. 4. The variation of fiber size with the Mn-content and roughness of ZnO thin films.

These nanofibers forming microfibers become thick in parallel with Mn-doping. As a result of this thickening, the size of the microfibers also increases, thereby increasing the surface roughness. The increase in surface roughness is caused by the fact that with Mn-doping, the dispersive properties of ZnO decrease [22] and the aggregation of nano-sized granules first form nanofibers, and microfibers are formed by the combination of these nanofibers. Moreover, the amount of Mn-doping causes significantly changes the surface roughness.

Table 1. Morphological parameters present work on ZnO nanolayers

	R_q (nm)	***Fiber size (µm)***
Pure ZnO	61.053	0.898
0.1% Mn doped ZnO	68.384	1.367
0.5 % Mn doped ZnO	71.534	1.628
1 % Mn doped ZnO	123.955	1.728
2 % Mn doped ZnO	169.251	2.292
5 % Mn doped ZnO	189.985	2.960

4. Conclusions

Mn: ZnO thin films were successfully produced with the sol-gel spin coating technique, a simple and effective method. The impact of Mn doping concentration on the morphological properties was discussed in detail. The micrographs obtained by AFM showed that the surface morphology was in the form of microfiber consisting of nanogranules and was significantly changed by Mn doping. It was found out that, as the Mn ratio increased, fiber sizes and surface roughness increased due to the increase

in grain sizes of the films. The morphological characteristics of films state that Mn2+ ions substitute for the Zn2+ ion without altering the wurtzite structure of ZnO. All these data confirm that Mn doping alters morphological properties.

The compliance to Research and Publication Ethics: This work was carried out by obeying research and ethics rules.

References

[1] Aydın, H., Yakuphanoglu, F., Aydın, C. „Al-doped ZnO as a multifunctional nanomaterial: Structural, morphological, optical and low-temperature gas sensing properties“. *Journal of Alloys and Compounds*, 773, 802-811, 2019.

[2] Aydın, C., Benhaliliba, M., Al-Ghamdi, A. A., Gafer, Z. H., El-Tantawy, F., Yakuphanoglu, F. "Determination of optical band gap of ZnO: ZnAl2O4 composite semiconductor nanopowder materials by optical reflectance method". *Journal of Electroceramics*, 31, 265-270, 2013.

[3] 3. Aydin, C. "Synthesis of Pd: ZnO nanofibers and their optical characterization dependent on modified morphological properties". *Journal of Alloys and Compounds*, 777, 145-151,2019.

[4] Aydin, H., Aydin, C., Al-Ghamdi, A. A., Farooq, W. A., Yakuphanoglu, F. “Refractive index dispersion properties of Cr-doped ZnO thin films by sol-gel spin coating method”. *Optik*, 127, 1879-1883,2016.

[5] Aydin, H., El-Nasser, H. M., Aydin, C., Al-Ghamdi, A. A., Yakuphanoglu, F. “Synthesis and characterization of nanostructured undoped and Sn-doped ZnO thin films via sol-gel approach”. *Applied Surface Science*, 350, 109-114, 2015.

[6] Aydın, C., Abd El-sadek, M. S., Zheng, K., Yahia, I. S., Yakuphanoglu, F. “Synthesis, diffused reflectance and electrical properties of nanocrystalline Fe-doped ZnO via sol–gel calcination technique”. *Optics & Laser Technology*, 48, 447-452, 2013.

[7] Aydın, C., El-Nasser, H. M., Yakuphanoglu, F., Yahia, I. S., Aksoy, M. “Nanopowder synthesis of aluminum doped cadmium oxide via sol–gel calcination processing”. *Journal of Alloys and Compounds*, 509, 854-858, 2011.

[8] Aydin, H., Tataroglu, A., Al-Ghamdi, A. A., Yakuphanoglu, F., El-Tantawy, F., Farooq, W. A. “A novel type heterojunction photodiodes formed junctions of Au/LiZnSnO and LiZnSnO/p-Si in series”. *Journal of Alloys and Compounds*, 625, 18-25, 2015.

[9] Aydin, C., Abd El-sadek, M. S., Zheng, K. B., Yahia, I. S., Yakuphanoglu, F. “Synthesis, diffused reflectance and electrical properties of nanocrystalline Fe-doped ZnO via sol-gel calcination technique”. *Optics and Laser Technology*, 48, 447-452, 2013.

[10] Rajalakshmi, R., Angappane, S. "Effect of thickness on the structural and optical properties of sputtered ZnO and ZnO: Mn thin films". *Journal of Alloys and Compounds*, 615, 355-362, 2014.

[11] Shinde, V. R., Gujar, T. P., Lokhande, C. D., Mane, R. S., Han, S.-H. “Mn doped and undoped ZnO films: A comparative structural, optical and electrical properties study”. *Materials Chemistry and Physics*, 96, 326-330, 2006.

[12] Soylu, M., Aydin, H., Al-Ghamdi, A. A., Farooq, W. A., Yakuphanoglu, F. “Study of optical and electrical assessments of the quaternary MgZnSnO system containing different Mg content”. *Journal of Materials Science: Materials in Electronics*, 25, 4235-4245, 2014.

[13] Aydın, C. “Synthesis of SnO2:rGO nanocomposites by the microwave-assisted hydrothermal method and change of the morphology, structural, optical and electrical properties”. *Journal of Alloys and Compounds*, 771, 964-972, 2019.

[14] Aydin, C., Aydin, H., Taskin, M., Yakuphanoglu, F. “A Novel Study: The Effect of Graphene Oxide on the Morphology, Crystal Structure, Optical and Electrical Properties of Lanthanum Ferrite Based Nano Electroceramics Synthesized by Hydrothermal Method”. *Journal of Nanoscience and Nanotechnology*, 19, 2547-2555, 2019.

[15] Aydin, C. “The functionalization of morphological, structural and optical properties of Fe doped SnO2 nanocrystals synthesized by the sol–gel method”. *Journal of Materials Science: Materials in Electronics*, 29, 20087-20096, 2018.

[16] Aydin, C. "Tin Oxide Based Nano Electroceramics Obtained from Sol&#8211, Gel Process: The Modified of the Structural and Opto-Electrical Properties with the Al Doping". *Journal of Nanoelectronics and Optoelectronics*, 13, 1460-1467, 2018.

[17] Aydin, H., Mansour, S. A., Aydin, C., Al-Ghamdi, A. A., Al-Hartomy, O. A., El-Tantawy, F., Yakuphanoglu, F. “Optical properties of nanostructure boron doped NiO thin films”. *Journal of Sol-Gel Science and Technology*, 64, 728-733, 2012.

[18] Aydın, C. “Variation of structural and electrical properties of gallium nitride-based nanomaterials with nickel dopant at different atomic ratios”. *Ceramics International*, 44, 17473-17478, 2018.

[19] Aydın, C., Mansour, S. A., Alahmed, Z. A., Yakuphanoglu, F. “Structural and optical characterization of sol–gel derived boron doped Fe2O3 nanostructured films”. *Journal of Sol-Gel Science and Technology*, 62, 397-403, 2012.

[20] Aydin, C., Al-Hartomy, O. A., Al-Ghamdi, A. A., Al-Hazmi, F., Yahia, I. S., El-Tantawy, F., Yakuphanoglu, F. “Controlling of crystal size and optical band gap of CdO nanopowder semiconductors by low and high Fe contents”. *Journal of Electroceramics*, 29, 155-162, 2012.

[21] Orhan, A., Aydin, C., Aydin, H., Al-Ghamdi, A. A., El-Tantawy, F., Yakuphanoglu, F. “Synthesis and optical properties of iron doped gallium nitride nanostructures by sol gel method”. *Microsystem Technologies*, 21, 1219-1224, 2015.

[22] Ganesh, V., Salem, G. F., Yahia, I. S., Yakuphanoglu, F. “Synthesis, Optical and Photoluminescence Properties of Cu-Doped Zno Nano-Fibers Thin Films: Nonlinear Optics”. *Journal of Electronic Materials*, 47, 1798-1805, 2018.

INESEG
INTERNATIONAL ENGINEERING, SCIENCE AND EDUCATION GROUP

Middle East Journal of Science

https://dergipark.org.tr/mejs

e-ISSN:2618-6136

MEJS

Research Article

A REVERSE HÖLDER INEQUALITY IN $L^{p(x)}(\Omega)$

Yasin Kaya

Dicle University Department of Mathematics, Diyarbakır, Turkey
ykaya@dicle.edu.tr

Abstract: *In this study, at first we provide a general overview of $L^{p(x)}(\Omega)$ spaces, also known as variable exponent Lebesgue spaces. They are a generalization of classical Lebesgue spaces L^p in the sense that constant exponent replaced by a measurable function. Then, based on classical Lebesgue space approach we prove a reverse of Hölder inequality in $L^{p(x)}(\Omega)$. Therefore, our proof in variable exponent Lebesgue space is very similar to that in classical Lebesgue space.*

Keywords*: Variable exponent Lebesgue space, measure, Radon–Nikodym derivative*

Received: November 18, 2019 Accepted: June 18, 2020

1. Introduction

Variable exponent Lebesgue spaces $L^{p(x)}(\Omega)$ are certain cases of Orlicz–Musielak spaces, and at this point of view investigation of $L^{p(x)}(\Omega)$ date back to Hudzik [1] and Musielak [2]. But historically a paper by W**.** Orlicz can be considered as the originating paper in this field [3]. These important spaces are also known as generalized Lebesgue spaces. Since $L^{p(x)}(\Omega)$ space is a natural generalization of the classical $L^p(\Omega)$ space , therefore, the first question which comes to mind is: what types of properties $L^p(\Omega)$ space can be transferred to $L^{p(x)}(\Omega)$ space? Variable exponent Lebesgue spaces have found applications in many areas of mathematics**,** physics and differential equations. To name few of those application**s** areas: modeling electrorheological fluids, image restoration, the calculus of variations, the analysis of quasi-Newtonian fluids, partial differential equations, fluid flow in porous media, For various and concrete applications of these spaces we refer to [4-9]. For further, and more detailed properties of $L^{p(x)}$ spaces we refer to [10-12]. Next we introduce some notations**,** present some fundamental definitions and recall some basic results of $L^{p(x)}$ spaces. In this paper, a variable exponent function means a measurable bounded function such that $p(.):\Omega\to[1,\infty)$. p^+ and p^- notations stands for

$$p^+ = ess\sup\{p(x):x\in\Omega\},\quad p^- = ess\ \inf\{p(x):x\in\Omega\}.$$

We give modular functional $\rho_{p(x)}(\phi)=\rho(\phi):L^{p(x)}(\Omega)\to\mathbb{R}$ such that

$$\rho(\phi)=\int_{\Omega}\left|\phi(x)\right|^{p(x)}dx.$$

The space $L^{p(x)}(\Omega)$ is defined in the following way:

$$L^{p(x)}(\Omega)=\left\{\phi:\Omega\to\mathbb{R}\text{ measurable}:\int_{\Omega}\left|\phi(x)\right|^{p(x)}dx<\infty\text{ holds}\right\}.$$

Then $L^{p(x)}(\Omega)$ is a Banach space under the Luxemburg norm

$$\left\|\phi\right\|_{L^{p(x)}(\Omega)}=\left\|\phi\right\|_{p(x)}=\inf\left\{\omega>0:\int_{\Omega}\left|\frac{\phi(x)}{\omega}\right|^{p(x)}dx\le 1\right\}. \tag{1}$$

If $p^{+}<\infty$, then in $L^{p(x)}(\Omega)$ space, the following inequality estimates a strong relationship between the modular functional and the norm

$$\min\left\{\left(\rho(\phi)\right)^{\frac{1}{p^{+}}},\left(\rho(\phi)\right)^{\frac{1}{p^{-}}}\right\}\le\left\|\phi\right\|_{p(x)}\le\max\left\{\left(\rho(\phi)\right)^{\frac{1}{p^{+}}},\left(\rho(\phi)\right)^{\frac{1}{p^{-}}}\right\}.$$

If $p(x)=p$ (constant) for all $x\in\Omega$, then space $L^{p(x)}(\Omega)$ agree with the classical Lebesgue space $L^{p}(\Omega)$ and these two norm values are equal. The topology of the function space $L^{p(x)}(\Omega)$ supplied with the norm (1) is equivalent to the topology of modular ρ convergence if and only if $p^{+}<\infty$. Notion of conjugate exponent from the classical case can be generalized to variable case by the similar formula

$$\frac{1}{p(x)}+\frac{1}{q(x)}=1$$

For any measurable function $\phi\in L^{p(\cdot)}(\Omega)$ and $\varphi\in L^{q(\cdot)}(\Omega)$ the Hölder like inequality

$$\int_{\Omega}\phi(x)\varphi(x)\,dx\le\beta\left\|\phi(x)\right\|_{p(x)}\left\|\varphi(x)\right\|_{q(x)}$$

holds.

We use the sign $\left|\Omega\right|$ to indicate the Lebesgue measure of a set $\Omega\subset\mathbb{R}^{n}$. Following shows us that when the exponent $p(x)$ is bounded then almost every $x\in\mathbb{R}^{n}$ is a Lebesgue point. This is shown in [13]. For $x\in\mathbb{R}^{n}$ and $t>0$, $B(x,t)$ stand for the open ball having center x and radius t. Let $p^{+}<\infty$. $\phi\in L^{p(x)}(\mathbb{R}^{n})$ then

$$\lim_{t\to 0}\frac{1}{|B(x,\ t)|}\int_{B(x,\ t)}|\phi(y)-\phi(x)|^{p(y)}dy=0$$

for almost every $x\in\mathbb{R}^n$.

For two functions ϕ and φ defined in $\mathbb{R}^n$, the convolution of ϕ and φ, denoted by $\phi*\varphi$, given by the formula:

$$\phi*\varphi(x)=\int_{\mathbb{R}^n}\phi(x-y)\varphi(y)\,dy$$

A useful inequality for convolution is Young's inequality. The Young's inequality is not true with full generality in $L^{p(\cdot)}$:

$$\|\phi*\varphi\|_{p(x)}\le\alpha\|\phi\|_{p(x)}\|\varphi\|_1$$

the inequality is valid if and only if $p(x)$ is constant.

2. Methods

Since the result that we wanted to prove was proved in general measure space rather than Lebesgue measure in classical Lebesgue spaces, we also state and prove our result in general measure space. Thus, by means of classical the $L^p(\Omega)$ approach we prove the following theorem.

Lemma 2.1. Let (X,M,ν) be a σ- finite measure space such that $\nu(X)=\infty$. Then there exists a measurable function $\psi\notin L^1(X,M,\nu)$ and $\psi\in L^{q(x)}(X,M,\nu)$ for all measurable variable exponent $q(x)$ satisfies q^->1 and $q^+<\infty$ conditions.

Proof. There exists disjoint sets A_1, A_2, A_3, … in M such that $1\le\nu(A_k)<\infty$ for each k and $X=\bigcup_{k=1}^{\infty}A_k$. Define $\psi(x)=\frac{1}{k.\nu(A_k)}$ on each A_k.

Now we have

$$\int_X|\psi|d\nu=\sum_{k=1}^{\infty}\int_{A_k}|\psi|d\nu=\sum_{k=1}^{\infty}\frac{1}{k}=\infty$$

This means that $\psi\notin L^1(X,M,\mu)$.

For $1<q^-\le q(x)\le q^+<\infty$, also we have

$$\begin{aligned}\int_X |\psi|^{q(.)} d\nu &= \sum_{k=1}^{\infty} \int_{A_k} |\psi|^{q(.)} d\nu \\ &= \sum_{k=1}^{\infty} \int_{A_k} \frac{1}{k^{q(.)}.\left[\nu\left(A_k\right)\right]^{q(.)}} d\nu \\ &\le \sum_{k=1}^{\infty} \int_{A_k} \frac{1}{k^{q^-}.\nu\left(A_k\right)} d\nu \\ &\le \sum_{k=1}^{\infty} \frac{1}{k^{q^-}} < \infty\end{aligned}$$

This means that $\psi \in L^{q(.)}\left(X, M, \nu\right)$.

3. Results

Theorem 3.1. Let $\left(X, M, \mu\right)$ be a σ - finite measure space such that $\mu\left(X\right) = \infty$. Assume a measurable variable exponent $p\left(x\right)$ satisfies $p^- > 1$, $p^+ < \infty$ conditions and $|\phi|$ is finite μ - a.e. on X. If $\phi\varphi \in L^1\left(X, M, \mu\right)$ for each $\varphi \in L^{q(x)}\left(X, M, \mu\right)$ then $\phi \in L^{p(x)}\left(X, M, \mu\right)$.

Proof. By the method of contradiction, let us assume the opposite, namely that $\phi \notin L^{p(.)}\left(X, M, \mu\right)$. Let us, now, obtain a new measure on $\left(X, M\right)$ as follows

$$\nu\left(A\right) = \int_A |\phi|^{p(.)} d\mu \quad \text{for } A \in M .$$

Then ν is also a σ - finite measure due to $\left(X, M, \mu\right)$, σ - finite and $|\phi|^{p(.)}$ finite a.e., μ -on X. Also, by Radon–Nikodym derivative we have $d\nu = |f|^{p(.)} d\mu$. It is important to be aware $\nu\left(X\right) = \int_X |\phi|^{p(.)} d\mu = \infty$, since we assume $\phi \notin L^{p(.)}\left(X, M, \mu\right)$. By Lemma 2.1. there is a measurable function ψ satisfying $\psi \notin L^1\left(X, M, \nu\right)$ and $\psi \in L^{q(.)}\left(X, M, \nu\right)$. Let us consider a function φ on X as follows, $\varphi = \psi |\phi|^{p(.)-1}$.

$$\int_X |\varphi|^{q(.)} d\mu = \int_X |\psi|^{q(.)} |\phi|^{p(.)} d\mu = \int_X |\psi|^{q(.)} d\nu < \infty$$

This gives us $\varphi \in L^q\left(X, M, \mu\right)$. We have also

$$\int_X |\phi\varphi| d\mu = \int_X |\psi| |\phi|^{p(.)} d\mu = \int_X |\psi| d\nu = \infty$$

This gives us $\varphi\phi \notin L^1\left(X, M, \mu\right)$. Hence our assumption led to a contradiction, since we have assumed $\varphi\phi \in L^1\left(X, M, \mu\right)$, and thus ϕ must be an element of $L^{p(.)}\left(X, M, \mu\right)$ space.

4. Discussion

By applying the classical methods of constant case, we obtained a reverse of Hölder inequality in $L^{p(x)}(\Omega)$ space. However, the case $p^- = 1$ still remain open in this context.

The compliance to Research and Publication Ethics: This work was carried out by obeying research and ethics rules.

References

[1] Hudzik, H., "The problems of separability, duality, reflexivity and of comparison for generalized Orlicz–Sobolev spaces $W_M^k(\Omega)$", *Commentationes Mathematicae*, 21, 315–324, 1979.

[2] Musielak, J., Orlicz *spaces and modular spaces*, Springer, Berlin Heidelberg New York, 1983.

[3] Orlicz, W., "Über konjugierte Exponentenfolgen", *Studia Mathematica*, 3, 200–212, 1931.

[4] Růžička, M., *Elektrorheological fluids: modeling and mathematical theory*, Springer-Verlag, Berlin, 2000.

[5] Acerbi, E., Mingione, G., "Regularity results for stationary electro-rheological fluids", *Archive for Rational Mechanics and Analysis*, 164(3), 213-259, 2002.

[6] Aboulaich, R., et al., "New diffusion models in image processing", *Computers & Mathematics with Applications*, *56*, 4, 874-882, 2008.

[7] Chen, Y., et al., "Variable exponent, linear growth functionals in image restoration" *SIAM journal on Applied Mathematics***,** *66*, 4, 1383-1406, 2006.

[8] Zhikov , V.V., "Meyer-type estimates for solving the nonlinear Stokes system"**,** *Differential Equations*, 33, 1, 108–115, 1997.

[9] Amaziane, B., et al., "Nonlinear flow through double porosity media in variable exponent Sobolev spaces", *Nonlinear Analysis: Real World Applications*, 10, 4, 2521-2530, 2009.

[10] Kováčik, O., Rákosník, J., "On spaces $L^{p(x)}$ and $W^{k,p(x)}$", *Czechoslovak Mathematical Journal*, 41, 4, 592-618, 1991.

[11] Diening, L., et al., M., *Lebesgue and Sobolev spaces with variable exponents*, Springer, 2011.

[12] Cruz-Uribe, D.V., Fiorenza, A., *Variable Lebesgue spaces: foundations and harmonic analysis*, Springer Science & Business Media, 2013.

[13] Harjulehto, P., Hasto, P., "Lebesgue points in variable exponent spaces", *Annales Academiæ Scientiarium Fennicæ. Mathematica*, 29, 295–306, 2004.

INESEG
INTERNATIONAL ENGINEERING, SCIENCE AND EDUCATION GROUP

Middle East Journal of Science

https://dergipark.org.tr/mejs

e-ISSN:2618-6136

MEJS

Research Article

FATTY ACID CONTENTS OF TWO EDIBLE MUSHROOM SPECIES (*CYCLOCYBE AEGERITA* AND *HYGROPHORUS EBURNEUS*) COLLECTED FROM TOKAT REGION

***Handan ÇINAR YILMAZ*[1*]** ***Hakan IŞIK*[2]** ***Aydın Şükrü BENGÜ*[3]**
***İbrahim TÜRKEKUL*[4]**

[1*]Bingöl University, Vocational School of Health Services, Department of Medical Services and Techniques, Program of Medical Laboratory Techniques, Bingöl, Turkey
[2]Tokat M. Emin Saraç Anatolian Religious High School, Tokat, Turkey
[3]Bingöl University, Vocational School of Health Services, Department of Medical Services and Techniques, Program of Medical Laboratory Techniques, Turkey
[4]Gaziosmanpaşa University, Faculty of Arts and Science, Biology Department, Tokat, Turkey
[*] Corresponding author; h.platanus@gmail.com

Abstract: *Edible species of mushrooms, which grow naturally and have important ecological tasks, are collected and consumed as a foodstuff in our country as well as in many regions of the world. Many studies to determine the chemical structure of the mushrooms have revealed that they are valuable nutrient sources in terms of essential fatty acids, essential amino acids, vitamins, and minerals. It is especially preferred by people who are dieting because they are poor in terms of calories and fat. This study aimed to determine the fatty acid contents of Cyclocybe aegerita (V. Brig.) Vizzini and Hygrophorus eburneus (Bull.) Fr. Mushroom samples collected from the natural environment. Mushroom samples, which are the material of our study, were collected in Tokat during field trips. The analyzes were performed by GC-MS instrument after obtaining methyl esters of fatty acids. At the end of the studies, palmitic acid C16:0, stearic acid C18:0, oleic acid C18:1(n-9) and linoleic acid C18:2 (n-9-12) from C. aegerita samples; myristic acid C14:0, palmitic acid C16:0, palmitoleic acid C16:1 (n-9), stearic acid C18:0, oleic acid C18:1(n-9), linoleic acid C18:2 (n-9-12), and nervonic acid C24:1(n-9) from H. eburneus samples were determined in different proportions. The highest amount of fatty acid was found linoleic acid in C. aegerita with proportions of 54.33% and oleic acid in H. eburneus samples with proportions of 47.80%. In addition to also in both mushroom species, the total saturated fatty acid rate was higher than the total unsaturated fatty acid rate.*

Keywords: *Cyclocybe aegerita, GC-MS, Hygrophorus eburneus, Tokat, Fatty Acids*

Received: May 4, 2020 Accepted: June 25, 2020

1. Introduction

Mushrooms, as well as playing an important role in the destruction of organic matter in nature are also used as a source of food. Mushrooms have the low-fat content, also are nutritious in terms of high protein, vitamins, fiber, carbohydrates, and minerals they contain. They can be cultivated and used

extensively in alternative medicine. Dried mushrooms contain 17.5% protein, 2.9% fat mostly in the form of the linoleic acid and linolenic acid, 39.9 % carbohydrates, 10% minerals and provide several vitamins including C, D, K, and B complex vitamins (thiamin, riboflavin, nicotinic acid, biotin) [1, 2, 3, 4, 5].

Wild edible mushrooms are become more important to human daily life due to their nutritional and chemical composition. Besides these, they have also been reported as therapeutic foods, useful in preventing diseases such as hypertension, hypercholesterolemia, and cancer [6-14]. The lipids are essential biological molecules in cell structure and metabolisms. Besides lipids are more important in energy storage than the caloric energy, protein, or carbohydrates. Lipids play the major functions as critical structural components of biological membranes, provide readily available energy reserves, and serve as essential vitamins and hormones, however, aid in the solubilization of dietary lipids in human health and physiology [7]. In addition, wild edible mushrooms include important fatty acids contents that are mostly not synthesized in the human body. The linoleic fatty acid is reported as omega 6 (W-6), linolenic fatty acid as omega 3 (W-3). Omega 6 has important roles in blood circulation and omega 3 is considered the most valuable fatty acid and can be taken from only plants and animal nutrients. Fatty acid compositions have important effects on blood lipid profiles. Saturated fatty acids increase high-density lipoprotein (HDL) cholesterol and reduce low-density lipoprotein (LDL) cholesterol, triacylglycerol, and lipid oxidation [7]. In order to make an analysis of fatty acids with GC-MS, it needs to be derivatized. For this, methylation is often preferred. Gas chromatography is widely used as the most reliable method for the detection of fatty acid esters.

The wild-grown edible mushroom species have seen very variety in Turkey and they have very high potential to consuming and exporting [5]. In many countries, local people usually hunt and eat only known edible mushroom species. Whereas many edible mushroom species aren't known by people and not known medicinal and nutritional features too. So, more edible mushroom species should be introduced to the benefits of the human race. With this study, we want to introduce some wild edible mushroom species that have a very high measure of fatty acids that are very important to the human body.

2. Materials and Methods

2.1. Collection andidentification of mushroomsamples

The mushroom samples, whose fatty acid contents will be analyzed, were collected from different localities in Tokat province. Some features of the mushroom samples are shown in Table 1.

Table 1. Some features of the analyzed mushroom species

Species	Family	Localities	Habitat
C. aegerita	*Strophariaceae*	Tokat center, Taşlıçiftlikköyü 40º19'K,036º28'D, 640 m	On poplar stump
H. eburneus	*Hygrophoraceae*	Tokatcenter, Avlunlar village 40º32'K,036º43'D, 963 m	On calcareous soil inmixed woodland

The color photographs of the samples were taken in their natural environment, then the samples were brought to the laboratory and dried after taking the spore prints. The properties of the microscopic structures (spore and basidium structure and measures, cystidia and pileipellis hyphae structures, clamp

connection, etc.) of the mushroom samples were obtained from dry samples using some chemical dye sand a Nikon brand research microscope. The samples, whose ecological and morphological features were obtained, were identified with the help of the current literature [8, 9, 10, 11, 12, 13]. The authors of the mushroom names are listed according to the literature [14].

2.2. Fatty acid analysis

The fatty acid contents of mushrooms were analyzed at Bingol University Central Research Laboratory.

2.2.1. Derivatization of fatty acid

Christie [15] was followed in the preparation of methylesters of fatty acids, after some revisions. With some revision, Hara and Radin [16] were followed for lipid extraction. For this, the plant sample was homogenized in 10 mL of hexane/isopropanol (3: 2) and centrifuged at 5000 rpm for 10 min. The organic phase was removed and placed in the test tubes. Fatty acids need to be derivatized in order to be able to look at GC. Derivatization with methyl esters is often preferred. For this purpose, Christie (1990) method was preferred because it is practical and highly efficient.

According to this method: the lipid extract prepared above was taken out of the mouth-capped tubes to prepare methyl esters. 5 mL of 2% methanolic sulfuric acid was added and vortexed. This mixture was left to stand for 15 hours of methylation at 50 ° C. At the end of this period, the tubes were removed, cooled to room temperature, and vortexed with the addition of 5 mL of 5% NaCl. The fatty acid methyl esters (FAME) formed in the tubes were extracted with 5 mL of hexane and the hexane phase was taken up from the top and treated with 5 mL of 2% NaHCO3 and waited for 2 hours to separate the phases. The solvent of the mixture containing the methyl esters was then evaporated under nitrogen at 45 ° C and the fatty acids below the test tubes were dissolved in 1 mL of hexane and analyzed by GC-MS using amber GC vials.

2.2.2. Analysis of FAME

A gas chromatograph instrument with an FID and MS (GC-MS, Agilent 7890 GC/5970 MS Series-Santa Clara, CA, USA), and a high polarity capillary column (HP-88, 100 m × 0.25 mm, 0.20 um film (Partno: 112-88A7, Agilent, Santa Clara, CA, USA) was used for fatty acid analyzes. Helium was used as the carrier gas (helium at 1 mL min^{-1} at 120 ºC). The injector temperature was set at 250 ºC, and the detector temperature at 250 ºC. The oven temperature was initially set at 120 ºC for 2 min and then raised to 250 ºC at 5 ºC min^{-1}. Because the hold time is 16 minutes, the total analysis is 45 minutes. The detector gas was air set at 350 $mLmin^{-1}$, and hydrogenas was set at 35 $mLmin^{-1}$. The detector makes up gas was nitrogen at 35 $mLmin^{-1}$. Other conditions: split ratio is 1/10, the solvent delay time is 12 minutes, the injection volume is 1 uL. An injection system with auto sampler was used (Table 2). GC-FID and MS results were recorded simultaneously. The results were evaluated by pairing with the NIST and WHILEY libraries registered on the device. The FID detector was used to increase the reliability of the analysis.

Table 2. Condition of gas chromatography

Condition of Gas Chromatography	
Instrument	Agilent 7890
MS Series	5970 MS
Column	HP88, 100m ×0.25mm×0.20µm
Carrier gas (Helium)	1mL min^{-1} (constant flow)
Injector temperature	250 ºC
FID detector temperature	250 ºC
Dried airflow	350 mL min^{-1}
Hydrogen flow	35 mL min^{-1}
Nitrogen (make up)	35 mL min^{-1}
Split ratio	1/10
Solvent delay time	12 min.
Injection volume	1 µL
Oven initial temperature	120 ºC at 2 min. hold time
Final temperature	250 ºC at 5 ºC/min. and hold time 16 min.
Total time	45 min.
Cleaning procedure of injector	Before and after cleaning 3 times with hexane

3. Results and Discussion

In the present study, the fatty acids composition of the edible mushroom samples collected from Tokat's province was analyzed. The analyzes were performed by the GC-MS instrument after obtaining methyl esters of fatty acids. As a result of the analyzes, different rates of saturated and unsaturated fatty acids were determined. The results for the fatty acid profile, total saturated fatty acids (ΣSFAs), and polyunsaturated fatty acids (ΣUFAs) of analyzed mushrooms were shown in Table 3.

Table 3. Fatty acid composition of two wild edible mushrooms (%)

Retention Time (min)		Fatty Acid Type	*C. aegerita*	*H. eburneus*
19,845		Myristic acid C14:0	ND	0.32
21,765		Pentadecanoic acid C15:0	ND	ND
23,982		Palmitic acid C16:0	22.15	21.93
28,525		Stearic acid C18:0	9.62	3.15
		ΣSFAs	31.77	25.40

24,873		Palmitoleic acid C16:1 (n-9)	ND	1.14
29,320		Oleic acid C18:1 (n-9)	13.90	47.80
30,688		Linoleic acid C18:2 (n-9-12)	54.33	24.88
41,235		Nervonic acid C24:1 (n-9)	ND	0.41
		ΣUFAs	68.23	74.23

ND- not detected

Palmitic, stearic, oleic, and linoleic acid were found in the fruit body of *C. aegerita* samples with proportions of 22.15%, 9.62%, 13.90%, 54.33%, respectively. In the fruit body of *H. eburneus* samples; myristic, palmitic, stearic, palmitoleic, oleic, linoleic, and nervonic acid were determined with proportions of 0.32%, 21.93%, 3.15%, 1.14%, 47.80%, 24.88%, 0.41%, respectively. In our analysis, it has been observed that the most amount of fatty acid varies among the mushroom species. While the 41ajör fatty acid was linoleic acid in *C. aegerita* species with 54.33%, it was oleic acid in *H. eburneus* species with 47.80%. Also, the most saturated fatty acid type in the studied samples was palmitic acid ranged from 22.15% (*C. aegerita*) to 21.93% (*H. eburneus*). Myristic, palmitoleic and nervonic acid can only be detected in *H. eburneus* with proportions of0.32%, 1.14%, 0.41%, respectively. In both the species ΣUFAs were higher than ΣSFAs (Tablo 3). Especially unsaturated fatty acids are very important in human nutrition. Because some of these (such as linoleic acid) are not produced in the human body, they must be taken from the outside.

In a study to determine the chemical content on *Agrocybeaegerita* (Syn: *C. aegerita*) [17], about 24 fatty acid kind were found at different rates. In this study it was found that the most abundant fatty acid was linoleic acid (78.40%). The other rates are palmitic acid (13.07%), oleic acid (3.03%), and stearic acid (2.13%). The amounts of other fatty acids were found to be very low (<1%). In our study, linoleic, palmitic, oleic and stearic acid rates were similar to the results of this study. However, the amount of oleic acid determined in our analysis was higher than this study. Also, similar to our work, in this study, it was observed that ΣUFAs (82.07%) was higher than ΣSFAs (17.93%).

The other studies have been made to detect fatty acids on *Agrocybe cylindracea* (Syn: *Cyclocybe cylindracea*), a similar species with *C. aegerita* [18]. Similarly with our result, linoleic acid was the major fatty acid (66.72%) detected in their study, and other fatty acids were palmitic (15.23%), stearic (5.52%), oleic acid (1.84%). They also determined that ΣUFAs (71.96%) was higher than ΣSFAs (28.13%).

Edible mushrooms have become the preferred foods in recent years because they are low in fat but especially rich in unsaturated fatty acids. Therefore, many studies have been carried out in our country, as in the whole world, to determine the fatty acid content of these foods. Another study has been made on wild edible mushroom "*Bovista plumbea*" to determine its fatty acid profile [19]. As a result of this, they determined that the most abundant detected fatty acids were C21:0, C20:1, C22:0, C18, and isomers of C18. *Tricholomopsis rutilans* has been analyzed to determine the fatty acid contents [20]. Oleic, linoleic, palmitic and stearic acid were the highest rates of fatty acid detected with proportions of 39.04, 37.09, 17.14, 4.18%, respectively. Also, three wild mushrooms *Coprinopsis atramentaria*, *Laetiporus sulphureus*, and *Suillus luteus* were studied to detect the fatty acid profiles.

The main fatty acid was oleic acid with 33.94% in *L. sulphureus*, andlinoleic acid in *C. atramentaria* and *S. Luteus* [21].

The results of our study and earlier studies show that mushrooms that are collected from the natural environment and grown in the culture medium are particularly rich in unsaturated fatty acids.

4. Conclusion

In addition to being economical, edible mushrooms that grow naturally in woodland or meadow areas have become the preferred foodstuffs today due to the chemicals they contain and their medical and pharmacological effects such as anticancer, antioxidant or antimicrobial effects. Our country is very rich in terms of mushroom diversity besides plant diversity. Many studies are carried out to determine mushroom biodiversity. These studies have shown that very few of the edible mushrooms grown in a region are known and consumed by humans. *C. Aegerita* and *H. eburneus* macrofungi grown naturally are also not very known as edible mushrooms. The results of our study showed that these two mushroom species are rich in unsaturated fatty acids.

The compliance to Research and Publication Ethics: This work was carried out by obeying research and ethics rules.

Acknowledgment

We would like to thank Bingöl University Central Research Laboratory staff and managers for the chemical analysis of mushrooms. This study was presented as an oral presentation at the 1st International Malatya Applied Sciences Congress (20-22 December 2019, Malatya).

References

[1] Anderson, S.C., Cockayne, S., "*Clinical Chemistry Concepts and Application*", McGraw-Hill, Medical Publishing Division, 2003.

[2] Ayaz, F.A., Torun, H., Özel, A., Çöl, M., Duran, C., Sesli, E., Çolak, A., "Nutritional value of some wild edible mushrooms from Black Sea Region (Turkey)", *Turkish Journal of Biochemistry,* 36(3), 213-221, 2011.

[3] Pekşen, A., Kibar, B., Yakupoğlu, G., "Yenilebilir bazı Lactarius türlerinin morfolojik özelliklerinin, protein ve mineral içeriklerinin belirlenmesi", *OMÜ Zir. Fak. Dergisi*, 22(3), 301-305, 2007.

[4] Pekşen, A., Yakupoğlu, G., Kibar, B., "Some chemical components of *Lactarius pyrogalus* from diverse locations", *Asian Journal of Chemistry*, 20(4), 3109-3114, 2008.

[5] Demirbaş, A., "Concentrations of 21 Metals in 18 Species of Mushrooms Growing in the East Black Sea Region", *Food Chemistry*, 75, 453-457, 2001.

[6] Manzi, P., Aguzzi, A., and Pizzoferrato, L., "Nutritional value of mushroom widely consumed in Italy", *Food Chemistry*, 73, 321-325, 2001.

[7] Barros, L., Baptista, P., Correia, D.M., Casal, S., Oliveira, B., Ferreira, I.C.F.R., "Fatty acid and sugar compositions, and nutritional value of five wild edible mushrooms from Northeast Portugal", *Food Chemistry*, 105, 140-145, 2007.

[8] Bon, M., *The Mushrooms and Toad stools of Britain and North-Western Europe*, Hodder-Stoughton, London, 1987.

[9] Breitenbach J., Kränzlin F., *Fungi of Switzerland. Vol: 3, Boletes and Agarics 1. Part*, VerlagMykologia CH-6000 Luzern 9, Switzerland, 1991.

[10] Breitenbach, J., Kränzlin, F., *Fungi of Switzerland. Vol: 4, Agarics 2. Part*, Verlag Mykologia CH-6000 Luzern 9, Switzerland, 1995.

[11] Jordan, M., *The Encyclopedia of Fungi of Britain and Europe*, Frances Lincoln, London, 1995.

[12] Moser, M., *Keys to Agarics and Boleti*, Gustav Fischer Verlag, Stuttgart, 1983.

[13] Phillips, R., *Mushrooms and Other Fungi of Great Britain & Europe*, Pan Books Ltd., London, 1981.

[14] Kirk, P., *Index Fungorum*, URL:http://www.indexfungorum.org (accessed 25 March 2020), 2011.

[15] Christie, W.W., *Gas Chromatography and Lipids: A Practical Guide*,The Oily Press Ltd. Scotland, 1990.

[16] Hara, A., Radin, N.S., "Lipid extraction of tissues with a low-toxicity solvent", *Analytical Biochemistry*, 90, 420-426, 1978.

[17] Petrović, J., Glamočlija, J., Stojković, D., Ćirić, A., Barros, L., Ferreira, I.C.F.R., Soković, M., "Nutritional value, chemical composition, antioxidant activity and enrichment of cream cheese with chestnut mushroom *Agrocybe aegerita* (Brig.) Sing", *The Journal of Food Science and Technology*, 52(10), 6711–6718, 2015.

[18] Ergönül, P.G., Ergönül, B., Kalyoncu, F., Akata, I., "Fatty acid compositions of five wild edible mushroom species collected from Turkey", *International Journal of Pharmacology*, 8(5), 463-466, 2012.

[19] Durmaz, F., Aktaş, S., Şimşek Sezer, E.N., "*Bovista plumbea* Pers.'nın yağ asiti içeriklerinin incelenmesi", *Mantar Dergisi* ,8(2), 104-108, 2017.

[20] Işık, H., Türkekul, İ., Çınar Yılmaz, H., Bengü, A.Ş., "Determination of fatty acid profile and mineral contents of *Tricholomopsis rutilans* collected from Yozgat" *Anatolian Journal of Botany*, 3(2), 64-68, 2019.

[21] Bengü, A.Ş., "Some elements and fatty acid profiles of three different edible mushrooms from Tokat province in Turkey", *Progress in Nutrition*, 21-1, 189-213, 2019.